AN EXPERIMENTAL STUDY ON FLOW-INDUCED VIBRATION OF A SINGLE AND ADJACENT TUBES WITHIN A MODEL HELICAL COIL HEAT EXCHANGER

A Dissertation

by

MARILYN DELGADO

Submitted to the Office of Graduate and Professional Studies of
Texas A&M University
in partial fulfillment of the requirements for the degree of

DOCTOR OF PHILOSOPHY

Chair of Committee,	Yassin A. Hassan
Co-Chair of Committee,	N. K. Anand
Committee Members,	Rodolfo Vaghetto
	Elia Merzari
Head of Department,	Timothy Jacobs

May 2021

Major Subject: Interdisciplinary Engineering

ABSTRACT

The helical coil heat exchanger (HCHX) is a geometrically complex tube and shell heat exchanger design that is preferred over straight tube bundles due to its increase in heat transfer efficiency, compact design, and thermal stress flexibility. Previous studies have shown prominent flow phenomena within the shell-side of the heat exchanger such as vortex shedding. A helical coil heat exchanger model was designed and constructed to study the vibration response of a single and two adjacent tubes within the center of the bundle. Results from tests conducted at Re_{∞} = 7,500 showed that the addition of an adjacent vibrating tube either upstream or downstream slightly increased the frequency of the motion but stabilized the vibration response. Results also showed that increasing Reynolds numbers 3,800 to 8,300 maintained frequencies of vibration from 9.17 Hz to 10.84 Hz in the x-direction and 19.45 Hz to 21.96 Hz in the y-direction. Comparisons to correlations showed a fair agreement with Weaver's Strouhal Number equations. Safety standard equations to avoid fluid elastic instability show that the flow was within the unsteady region at even the lowest Reynolds numbers suggesting they do not accurately predict the flow development within this heat exchanger design.

DEDICATION

To the many people who believe I am more capable than I believe I am.

Thank you.

ACKNOWLEDGEMENTS

I would like to thank my committee chair, Dr. Yassin Hassan, for giving me the opportunity to pursue my research interests in an environment that provided the technical and emotional support to complete this doctorate degree. I appreciate the patience and motivation you have given me over my time here at Texas A&M. I hope that in whatever endeavors I pursue next, I will able to make a good impression as being a student from your research laboratory.

I would like to thank my committee co-chair, Dr. N.K. Anand, for his guidance and support throughout all the research endeavors I pursued. Especially during this past year, when there were times that many things were uncertain, your dedication to our weekly meetings helped maintain a sense of normalcy and vision to continue pursuing the research.

I would like to thank my committee member, Dr. Rodolfo Vaghetto, for his everyday guidance on all matters regarding the graduate student experience. Your technical expertise as well as your kindness have made my time at Texas A&M a lot easier.

I would like to thank my committee member, Dr. Elia Merzari, for his support for this research and prospective endeavors.

I would also like to thank the members of my research laboratory who not only, never complained directly to me about my laughter and noise level, but supported me

with hands on data acquisition or conversations that allowed me to develop my research in new ways.

Thanks also go out to the departmental faculty and staff of both the Nuclear Engineering and Multidisciplinary Engineering departments and the SSC staff at the University Services Building. During this pandemic, work has been made more difficult and seeing the additional effort all put in, reminded me to also work hard.

Finally, to my family and friends, I can't express how both stressful and wonderful this experience has been for me. When I was ready to quit – like actually ready to quit, not just being dramatic – you reminded me of the path ahead and gave me the encouragement and love needed to move forward. Thank you for being there for me.

CONTRIBUTORS AND FUNDING SOURCES

Contributors

This work was supervised by a dissertation committee consisting of Professor Yassin A. Hassan of the Department of Nuclear Engineering, Professor N.K. Anand of the Department of Mechanical Engineering, Professor Rodolfo Vaghetto of the Department of Nuclear Engineering and Professor Elia Merzari of the Department of Nuclear Engineering.

All work conducted for the dissertation was completed by the student independently.

Funding Sources

Graduate study and research was supported by the Texas A&M University Thermal Hydraulic Research Laboratory in the Nuclear Engineering Department.

NOMENCLATURE

a	transverse pitch ratio
A_t	tube material cross sectional area
b	lateral pitch ratio
C_m	added mass
CFD	computational fluid dynamics
D or D_R	rod (tube) diameter
D_C	clearance diameter
E	modulus of elasticity
fps	frames per second
F_{CR}	Euler Buckling Load
f_N	natural frequency
f_{TB}	turbulent buffeting frequency
f_V	vortex shedding frequency
FEA	Finite Element Analysis
FEI	Fluid Elastic Instability
g	gravity constant
HCHX	Helical Coil Heat Exchanger
I	moment of inertia
k	spring constant
L_i	tube span length
L_R	Tube length

m	effective mass per unit length
P	pitch
PSD	power spectrum density
r_1, r_2	radius
Re_∞	Reynolds Number using inlet velocity
St	Strouhal Number
S_T	transverse pitch
S_L	lateral pitch
TEMA	Tubular Exchangers Manufacturers Association
V or V_∞	inlet velocity
V_{CR}	critical velocity
V_g	gap velocity
~	approximately

Greek

δ	damping ratio
ζ	critical damping ratio
θ	angle
λ_n	frequency constant
μ	dynamic viscosity
π	constant pi
ρ or ρ_S	shell-side fluid density

σ_t	tube longitudinal stress
χ	mass-damping parameter
χ_B	axial stress factor

TABLE OF CONTENTS

Page

LIST OF FIGURES

Page

LIST OF TABLES

Page

1. INTRODUCTION

Tube and shell heat exchangers are a very common design of heat exchanger for applications across industry since its development in the early 1960s. A particular design that implements concentric coiling tube bundles is referred to as the Helical Coil Heat Exchanger (HCHX). This type of heat exchanger is preferred due to thermal stress flexibility, volumetric efficiency and increased heat transfer compared to conventional straight tube and shell heat exchangers [1]. The geometry of the model utilized in this study is derived from multiple HCHX designs proposed for use in the nuclear industry [2,3,4, and 5]. This design is unique due to its adjacent interlacing behavior where a column of tubes coils in the opposite direction and at a different helical pitch than the column of tubes adjacent to it. An example of this interlacing behavior compared to the standard tube bundle design is presented in Figure 1.1 The shell-side fluid transfers heat as it flows over the tubes that carry a secondary fluid. From Figure 1.1, it can be seen how the alternating helical pitch affects the cross-flow behavior of the shell-side flow.

Previous studies conducted at Texas A&M's Thermal Hydraulic Research Laboratory within the Nuclear Engineering department have isolated the shell-side fluid behavior and examined different phenomenon. A first set of experimental studies used particle image velocimetry to visualize flow fields where high frequency vortex shedding was characterized based on Reynold's number [6]. Another study examined the changes in pressure on the surface of the tubes using the experimental technique called pressure sensitive paint [7].

While increased turbulence of the shell-side flow is preferable to increase the heat transfer between the two fluids, there are structural design limitations to be considered. This study aims to compare the response of a single, and adjacent self-excited vibrating tubes within a model of this complex tube bundle geometry to currently existing correlations that aim to predict limitations of the system to avoid flow induced vibration. For this study, a test section was designed, constructed and implemented into a closed loop facility where a high-speed camera was used to capture the vibration induced by the flow around the tube bundle.

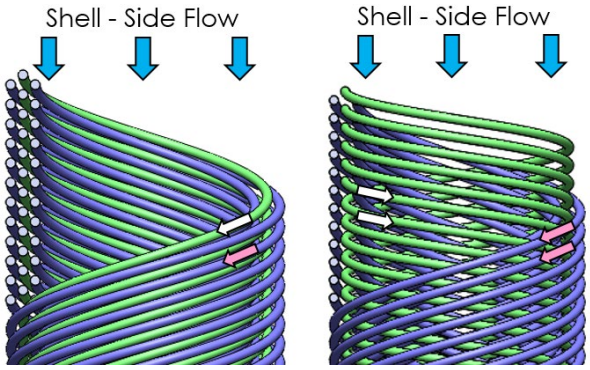

Figure 1.1 Different geometric designs of an (a) uniform helical pitch and (b) alternating helical pitch tube and shell heat exchanger.

1.1. Introduction to Flow-Induced Vibration

Fluid properties are quantified within the cross-flow area based on the tube pitch ratios and assume a constant helical body pitch. Tube pitches are defined by the direction of the flow over the tubes. The distance between the tubes in the same direction as the free stream flow is the lateral pitch, S_L. The transverse distance between tubes perpendicular to the free-stream flow is the transverse pitch or S_T. When these distances are divided by

the diameter of the tube, D, they become the transverse and lateral pitch ratios, a and b, respectively. A bundle is characterized by the product of $a \times b < 1.25$ to be compact or $a \times b > 4$ to be widely spaced. In particular, the most common tube pitch types for tube and shell heat exchangers are the in-line and staggered tube arrangements where an in-line square has a = b, rotated square has a = 2b, and parallel triangle has a= 2b/√3. Shown in Figure 1.2, these tube pitches are used to define the geometry when calculating heat exchanger properties such as pressure drop, heat transfer coefficient, and flow characteristics [8].

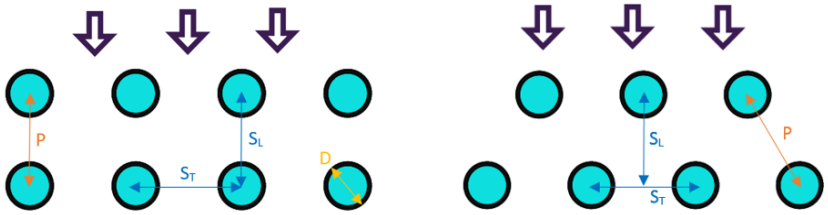

Figure 1.2 Characteristic geometric parameters of a tube bundle arrangement

$$a = \frac{S_T}{D} \quad \text{Eq 1.1}$$

$$b = \frac{S_L}{D} \quad \text{Eq 1.2}$$

A widely researched topic when designing tube bundles in cross-flow is the effect that the shell side flow has on the motion of the tubes, namely flow induced vibration (FIV). As the tube walls are generally thin, mechanical failures from fatigue, collision damage and tube joint failures can occur [9,10]. There are several mechanisms known to influence flow-induced vibration such as vortex shedding, turbulent buffeting, fluid elastic

instability, and acoustic resonance [11]. Acoustic resonance is generally considered when gases are utilized as the working fluid within the system. For single-phase flow systems, vortex shedding, turbulent buffeting, and fluid elastic instability are considered to induce FIV [11, 12].

The vortex shedding phenomena has been studied for lift and drag coefficients across a large range of Reynolds numbers for a single cylinder by Chen and Weber [13]. It was once thought that a tube bundle shared similar characteristics with a single cylinder, nevertheless, similarities were only found within the first few rows of tube bundles with specific lateral and transverse pitch ratios [11]. An important parameter to study vortex shedding is defined by the non-dimensional parameter, Strouhal Number, St, where f_V is the vortex shedding frequency, and V_g is the gap velocity.

$$St = \frac{f_v D}{V_g} \quad \text{Eq 1.3}$$

Researchers such as Chen [14] and Fitz-Hugh [15] created Strouhal maps for a large variety of various pitch ratios. Chen's maps have been widely accepted in industry as the standard and have been used by the Tubular Exchangers Manufacturers Association (TEMA). Correlations from experimental data were also developed by Zukauskas [16] and Weaver et al [17]. Weaver's correlations for Strouhal Number are defined by the pitch ratio, P/D, of the tube bundle for the following tube bundle patterns.

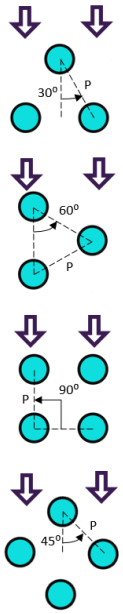

Normal Triangle (30^0) $St = \frac{1}{1.73\frac{P}{D}}$ Eq 1.4

Parallel Triangle (60^0) $St = \frac{1}{1.16\frac{P}{D}}$ Eq 1.5

Normal Square (90^0)

Rotated Square (45^0)

$St = \frac{1}{2\frac{P}{D}}$ Eq 1.6

Studies from Blevins [18] and Zukauskas [16] showed that in a closely packed tube bundle geometry, vortex shedding becomes less structured and can be better characterized as turbulent buffeting deep within the tube bundle. Turbulent buffeting can be described as when vortex shedding degenerates into broad range turbulent eddies rather than a single distinct frequency. Turbulent buffeting was researched extensively for tube bundles by Owen [19]. His experimental work resulted in an expression for the dominant central frequency of turbulent buffeting. This correlation had been reviewed by Weaver and Grover [20] to be the most reliable when the minimum gap velocity is used and the transverse pitch ratio, a, is greater than 1.25. Although this expression is included in TEMA's standards, the correlation has not been validated for liquids; therefore, it is suggested for gases only [11].

$$f_{TB} = \frac{V}{Dab}\left[3.05\left(1-\frac{1}{a}\right)^2 + 0.28\right] \quad \text{Eq 1.7}$$

Fluid Elastic Vibration (FEV) or Instabilities (FEI) sets in at a critical velocity for a tube bundle. FEI has been found to lead to wear and destruction of steam generator tubes [21]. When the flow velocity around the tube bundle is high enough that the energy absorbed from the fluid forces exceeds the energy dissipated by the dampening, FEI occurs. Researchers such as Connors [22] began to study the stability criterion for tube bundles as a semi-empirical model to determine a critical flow velocity, V_{CR}. His experimental studies linked the critical velocity to the natural frequency, f_N, and mass-damping parameter, χ, of the bundle. Chen also recommended a critical velocity that he later revised for specific tube bundle orientations, presented as Eq 1.8. and is included in TEMA [23].

$$\frac{V_{CR}}{f_N D} = A\chi^B \qquad \text{Eq 1.8}$$

$$\chi = \frac{m\delta}{\rho_S D^2} \qquad \text{Eq 1.9}$$

$$\delta = 2\pi\zeta \qquad \text{Eq 1.10}$$

where A, B and C are constants dependent on the pitch ratio of the tube bundle, m is the effective tube mass per unit length, ρ_S is the shell-side fluid density and ζ is the critical damping ratio. For shell-side liquid flow, TEMA recommends to choose the greater value from the two equations for damping parameter, δ. Note that equations 1.11a and 1.11b use U.S customary units.

$$\delta_1 = \frac{3.41D}{mf_N} \qquad \text{Eq 1.11a}$$

$$\delta_2 = \frac{0.012D}{m}\left(\frac{\rho_S\,\mu}{f_N}\right) \qquad \text{Eq 1.11b}$$

Chen's criterion differs from Connors as it includes the tube pitch ratio for staggered tube bundles. Au-Yang et al. [24] developed their own criteria with a conservative guideline when designing tube bundles that is currently implemented in ASME Code, Section III. Pettigrew and Taylor [25] conducted a parametric study on FEI of a flexible tube bundle in cross-flow to develop their own design criteria for critical velocity. Depending on the design criteria, each of these developed correlations can be used. Each correlation takes the form of Eq 8 with different constants. Nevertheless, the criteria to avoid FEI remains that $V_{CR} > V_g$.

From the discussion of FEI, a frequency that is critical to the design and operation of a tube and shell heat exchanger is the natural frequency of the tube bundle, f_N. The lowest frequency at which tubes vibrate is known as its natural frequency. When the exciting frequency matches the natural frequency, this is known as resonance. The natural frequency of a tube bundle depends on the geometry, material properties, damping and tube-to-support connections. Correlations exist for the two most common tube bundle configurations: straight tube bundles and U-tube bundles. As this study looks at straightened tubes representative of the HCHX design, the natural frequency equation for straight tubes will be considered. A widely accepted correlation that considers each span between tube supports was developed by Timoshenko and Young [26]. Natural frequencies for each span are calculated and the lowest frequency of the spans is taken as the representative frequency for the entire tube bundle. Equation 1.12 shows the natural

frequency as a function of the axial stress factor, χ_β, the frequency constant, λ_n, and span length, L_i.

$$f_N = \frac{1}{2\pi}\frac{\chi_\beta \lambda_n^2}{L_i^2}\left(\frac{EIg_c}{m}\right)^2 \quad \mathrm{N} = 1, 2, 3, \ldots \qquad \text{Eq 1.12}$$

$$\chi_\beta = \sqrt{1 \pm \frac{A_t \sigma_t}{F_{CR}}} \qquad \text{Eq 1.13}$$

Where E is the modulus of elasticity of the tube material, I is the moment of inertia of the cross section, A_t is the tube material cross sectional area, σ_t is the tube longitudinal stress and F_{CR} is the Euler buckling load.

1.2. Literature Review

As discussed, there are many researchers who have contributed to the development of conceptual aspects and correlations of flow-induced vibration within tube bundles. Since then, advancements in experimental techniques and manufacturing methods have allowed more complex geometries to be studied in relation to flow induced vibration. Table I summarizes more recent works of research that are or include experimental investigations and shows how varied the geometry of the tube bundles between the studies are.

Table 1.1 A summary of recent studies for flow induced vibration in tube bundles.

Authors	Year	Type of Study	Test Conditions
Weaver, Zaida, Au-Yang, Chen, Paidoussis, Pettigrew [27]	2000	Overview	
Inada, Kawamura, Yasuo, Yoneda [28]	2002	Experimental Forced vibration Two Phase	Water & Air Cylinder tubes Square array P/D = 1.42
Inada, Nishihara, Yasuo, Morita, Sakishita, Mizutani [29]	2003	Experimental Self-excited vibration Single Phase	Water Cross-shaped tubes Square & staggered array P/D = 1/10
Goyder [30]	2003	Overview	
Catton, Dhir, Mitra, Alquaddoomi, Adinolfi [31]	2004	Experimental Self-excited vibration Single & two-phase	Water & steam Cylindrical tubes Square array P/D = 1.2, 1.4, 1.55
Lin, Yu [32]	2005	Experimental Self-excited vibration Single phase	Water Cylinder tubes Rotated triangle array P/D = 1.33
Païdoussis [33]	2006	Overview	
Sawadogo, Mureithi [34]	2014	Experimental Self-excited Vibration Two Phase	Water & Air Cylinder Tubes Rotated Triangle Array P/D = 1.5
Annamalai, Karuppasamy [35]	2016	Experimental Self-excited Vibration Single Phase	Air Cylinder Tubes Normal Triangle Array P/D = 1.85
Marcum, Harmon [36]	2016	Experimental Self-excited Vibration Single Phase	Water Cylinder Tubes Helical Coil Array P/D = 1.2, 1.4, 1.6, 2.0
Elhelaly, Hassan, Mohany, Moussa [37]	2017	Experimental Self-excited Vibration Single Phase	Air Cylinder Tubes Triangle, Square Array P/D = 1.5, 1.733
Yuan, Solberg, Merzari, Kraus, Grindeau [38]	2017	Nek5000 CFD Self-excited Vibration Single Phase	Water Cylinder Tubes Helical Coil Array

Table 1.1 Continued

Authors	Year	Type of Study	Test Conditions
da Silva, Luciano, Utzig, Meier [39]	2018	Experimental Self-excited Vibration Single Phase	Water Cylinder Tubes In-line Array $S_T/D = 1.5, 3$ $S_L/D = 2, 4$
Chen, Ji, Williams, Xu, Yang, Cui [40]	2018	CFD Self-excited Vibration Single Phase	Cylinder Tubes In-line Array $S_L/D = 1.2, 1.5, 2.0, 3.0, 4.0, 5.0$
Yin, Passano, Larsen [41]	2018	Experimental Forced Vibration Single Phase	Water Cylinder Tubes Single Rod
Cioncolini, Silva-Leon, Cooper, Quinn, Iacovides [42]	2018	Experimental Self-excited Vibration Single Phase	Water Cylinder Tubes Single Rod
Alvarez-Briceno, Kanizawa, Ribatski, de Oliveira [43]	2018	Experimental Self-excited Vibration Two-Phase	Air & Water Cylinder Tubes Normal Triangle Array P/D = 1.26
Han, Ma, Xu, Zhang [44]	2018	Experimental Self-excited Vibration Single Phase	Air & Water Cylinder Tubes Side by Side Array P/D = 3.0, 4.0, 6.0, 8.0
Tang, Bao, Lv, Cui, Luo, Xu [45]	2019	ANSYS Fluent CFD Self-excited Vibration Single Phase	Steam Cylinder Tubes Triangle Array P/D = 1.633
Wang, Xu, Yu, Wang, Zhou, Incecik [46]	2019	Experimental Self-excited Vibration Single Phase	Water Cylinder Tubes In-line Array $S_T/D = 8.0$
Tang, Liu, Ding, Zhu, Yuan [47]	2020	CFD/CSD Self-excited Vibration Single Phase	Steam Cylinder Tubes Normal Triangle Array P/D = 1.633

While Table 1.1 is just a fraction of the studies that have been done in the past years related to tube and shell heat exchanger systems and flow-induced vibration, it provides insight to the increase in interest between the early 2000s and late 2010s.

During this time, advanced nuclear reactor designs were proposing to use the helical coil heat exchanger as the main heat exchanger of the system, promoting researchers to investigate complex flow phenomena for computational fluid dynamic (CFD) validation [2,3,4, and 5]. Table 1.1 also shows the difference in geometry nomenclature between studies. Studies vary between using the pitch ratio, P/D, and the lateral and transverse pitch ratio, S_T and S_L, respectively, due to the difference in variables within correlations relating the tube bundle geometry to heat transfer and fluid characteristics. As a heat exchanger is not only utilized in multiple industries, such as nuclear and chemical, there are also studies that look at tube bundles/arrays from underwater ocean engineering applications. Therefore, the difference in defining geometric lengths is only one of the many conflicting terms utilized within studies of cross-flow around tube bundles and flow-induced vibration.

1.3. Introduction to the Helical Coil Heat Exchanger (HCHX)

While different types of tube and shell heat exchangers have been developed, the concept of coiling tube bundles has been predominantly developed and used in two industries: cryogenics and nuclear power. While for this study, we have been referring to this design as the Helical Coil Heat Exchanger (HCHX), the design is also known by several different names based on the industry that utilized it and its direct function. In cryogenics this design has been identified as a Coiled Tube Evaporator [48], Coil Wound Heat Exchanger (CWHE) [49], Spiral Wound Heat Exchanger (SWHE) [50], and Spool-Wound Heat Exchanger [51]. For the process of liquefied natural gas (LNG),

pressurized feed gas is cooled down from room temperature to -162ºC with refrigerant. These cryogenic conditions combined with the large surface area between both fluids makes a Helical Coil Heat Exchanger ideal.

In nuclear power, the design has been referred to as a Helical Tube Intermediate Heat Exchanger (Helical Tube IHX) [52], Helical Coil Steam Generator (HCSG) [3], and similarly to cryogenics, Coil-Wound Heat Exchanger [53]. Since the 1960's, the nuclear power industry has been designing and testing different types of coiling heat exchangers. Nuclear power plants constructed during this time utilized U-Tube tube and shell heat exchangers, therefore improving on this design, the helical coil tube bundles increased the surface area between the two fluids and allowed for higher thermal stress flexibility. While most nuclear power reactors were constructed by 1974, an accident at Three Mile Island and changing economics halted the construction of new nuclear power plants, and no improvements or changes were passed through the Nuclear Regulatory Commission until 2012. Development of new heat exchanger designs also took a back seat in nuclear power research during this time. The combination of small modular and next generation nuclear reactors proposing to use this design and the advancements in computational thermal hydraulics to discretize small scale turbulent flow phenomena, has brought the design back to the forefront of research in the past decade.

This study identifies the design of the heat exchanger as the Helical Coil Heat Exchanger due to the popularity of this term emerging in recent years for cryogenic [49, 50], solar power [54], and next generation nuclear power from which the particular geometry was modeled after [2, 3, 4, 5].

2. EXPERIMENTAL METHOD

2.1. Test Section Development

As introduced, the HCHX is a unique design that incorporates coiling tube bundles. In order to study the shell-side behavior of the geometry, the test section designed uses rods in place of the tubes found in the actual heat exchanger. Therefore, the term tube and rod will be used interchangeably.

Using the available public literature at the time of this work, a model was created that incorporated design features from multiple proposed HCHX within the nuclear field [2, 3, 4, 5]. Using a multi-layered coiling bundle design, a model was created that incorporated five alternating pitch tube bundles. While some engineering applications choose to scale down for experimental studies, for this study, the vibration is studied from a section of a one-to-one representation using the tube diameter typically found in the heat exchanger. The five tube bundles create the rod columns and rows shown in Figure 2.1. Three columns of 18 rods are at a +4-degree inclination, and two rod-bundles of 9 rods are at a -9-degree inclination. The ends of the test section were chosen to represent a segment between brackets meant to hold the tubes in place in a full-scale design [38]. Figure 2.1 shows the development of the section taken from an HCHX design to the test section constructed for this study.

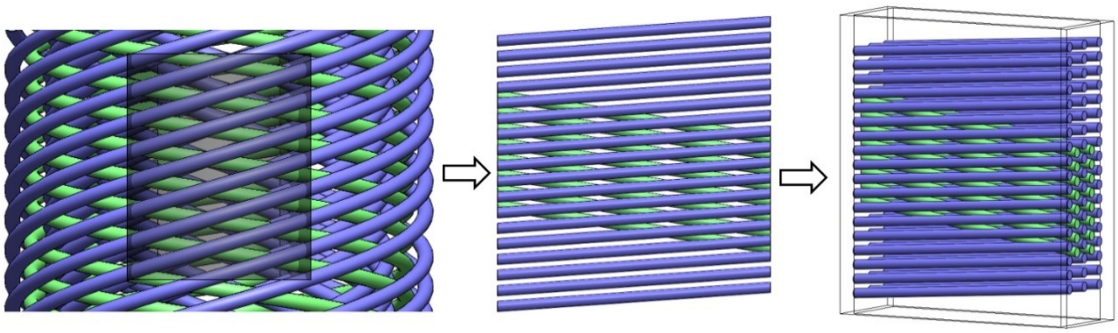

Figure 2.1 Derivation of the model test section from a full-scale HCHX

From the model shown in Figure 2.1, a test section was designed to study the vibration of one or two adjacent rods that are located at the center of the tube bundle. Based on the literature review, these rods were selected to be the most representative of the general fluid behavior within the shell-side, avoiding entrance and exit effects [31]. The rods chosen to vibrate were Rod 9 and Rod 10 from the center tube bundle that is angled +4 degrees from left to right. In order to experimentally capture the motion of the rods, a see-through module that would allow for vibration and visualization was designed. A camera would capture the motion of the tubes outside of the vibration modules on either end of the tubes. Springs would be used to mechanically act as a baffle or bracket intended to hold the tube in place and provide resistance to any flow-induced vibration. The conceptual design of the test section and the vibration modules attached is seen in Figure 2.2.

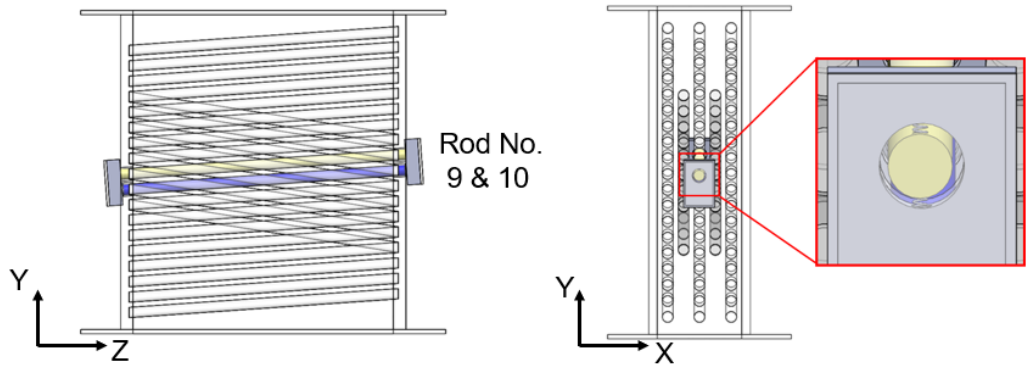

Figure 2.2 Conceptual test section with vibration modules.

2.1.1. Determination of Rod Clearance and Spring Rate

Under normal operation conditions of a system, the limit of vibration is generalized based on the maximum allowable deflection, meaning, if you give the tube clearance, you should expect it to reach that maximum clearance during operation. Therefore, in order to have limitations for the vibration within the test section, a simple finite element analysis (FEA) analysis was conducted using a model from a proposed nuclear small modular reactor design [55].

Using an estimated flow rate within the system to determine the fluid force acting on a single tube within the tube bundle, a simple finite element analysis (FEA) using SOLIDWORKS Simulation was conducted to get a general estimate of the allowed deflection within these support structures around a tube bundle. The support assembly used as an example uses three tabs, one above and two below, to hold each tube at each radial location in place. Therefore, only an estimated pressure could be determined for the force acting on a tab. A pressure of 65.9 psi was applied to the end of the tab, while the top end was considered fixed. Figure 2.3 shows the levels of mesh refinement with the imposed conditions on the support tab where the green arrows represent the fixed

end and the orange arrows represent the pressure. A nodal sensitivity test was conducted until the variance was less than 1%. The results of the convergence test showed that ~ 25,000 nodes was enough to reach a constant deflection of 2.55 mm, as seen in Figure 2.4. A full description of the study can be found in Appendix A.

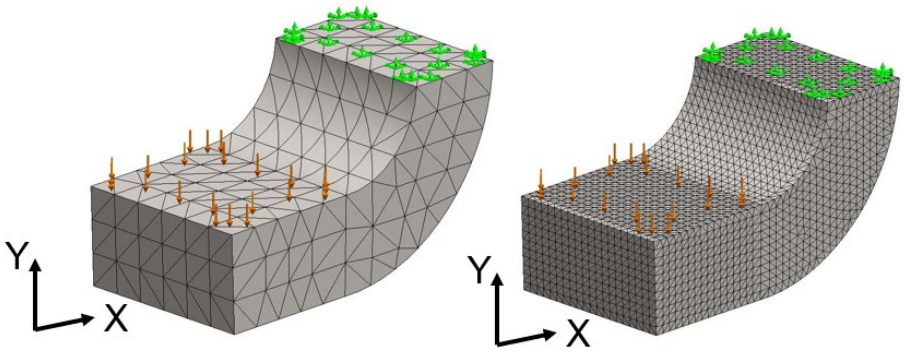

Figure 2.3 Mesh refinement for the support tab used as an estimate for allowable deflection within the test section.

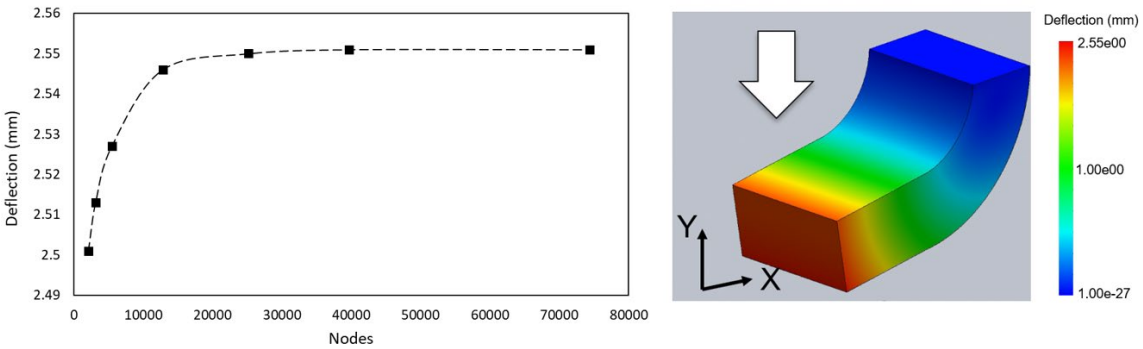

Figure 2.4 Nodal sensitivity analysis and final assessment deflection used to determine allowable clearance around rod within the test section.

In order to match the allowable motion in the y-direction, two springs were utilized. In order to use springs within the system but not implement an intrusive device to the system, the modules and vibrating rod ends were created to house the springs.

Initially, the modules were designed to house the springs at every 90 degrees around the rod. Figure 2.5 shows the initial module design and machining of the rod to hold the springs. Nevertheless, due to the tight tolerances around the rod, the springs were chosen to sit above and below the rod maintaining the resistance in the y-direction. The springs were the same material, SS316, as the support tabs and have a compression rate of 262.7 N/m or 1.5 lbs./in as rated by their manufacturer. For all experiments, the same types of springs were used changing them to new springs before each set of experimental conditions.

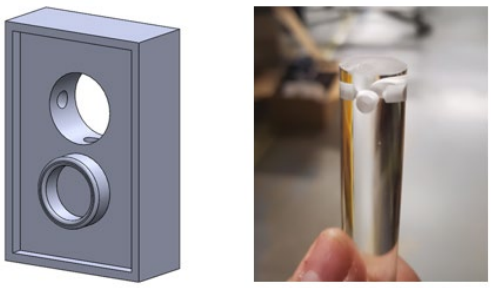

Figure 2.5 CAD vibration module design and rod end to fit the springs

The rod ends, as shown in Figure 2.5 were machined with a mill and jig that allowed the rod to be rotated every 90º. The test section was mainly manufactured in-house using acrylic and rods cut to size from the supplier. Figure 2.6 shows the side walls of the test section with the ports for the free vibrating rods as well as the process of putting the rigid rods within the test section. Each side was machined to have one protruding end as to make a miter joint in order to reduce the potential for leaks. Two types of acrylic adhesive with different densities were used to weld and fill gaps between adjoining walls and flanges.

Due to the needed accuracy of the vibration modules, as they dictate the allowable area of vibration, the modules were 3D- printed using polyethylene terephthalate with a glycol modification (PETG) with 100 μm layers and 80% fill. The diameter of the clearance for the rod is 2.09 cm ± 0.02 cm. Two different modules were created based on the number of rods allowed to vibrate. One module holds one rod in place with protrusions and the second one allows both to vibrate with the same clearance. The printed modules are shown in Figure 2.7. Depending on the set of experiments that were ran, the modules on both sides of the test section could be changed or inverted.

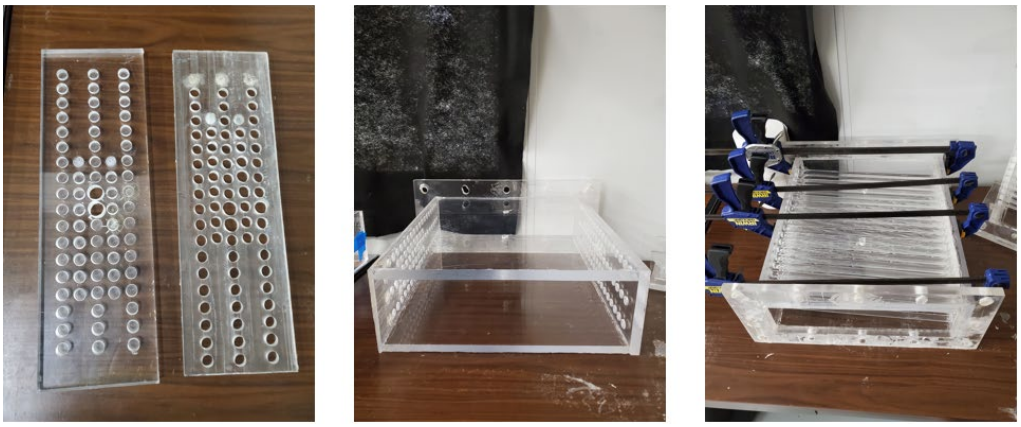

Figure 2.6 Construction progression of the Test Section with rigid rods and flanges all made from acrylic.

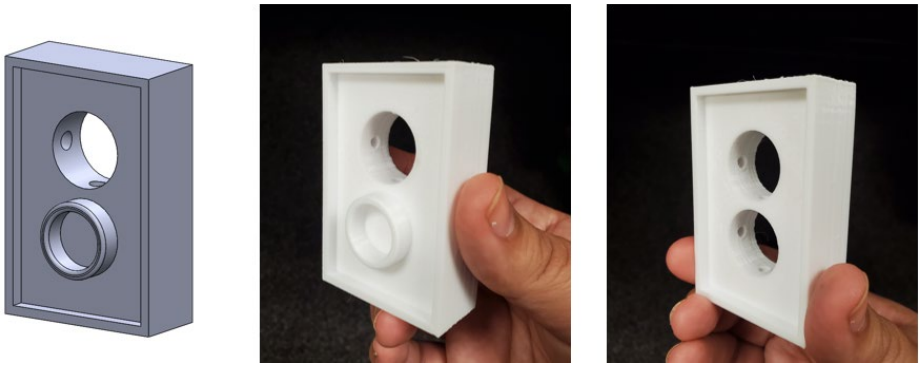

Figure 2.7 Two types of vibration modules meant to allow a single and two rods vibrating

2.2. Test Facility Construction

In order to move the working fluid through the test section, a closed loop facility was created around the test section. In order to attain particular flow rates at the inlet of the test section, a tank with a volumetric capacity of approximately 25 gallons feeds into a centrifugal pump. The centrifugal pump was selected to provide enough vertical head to the upper plenum of the test facility that provides an inlet velocity, V_∞, up to 0.5 m/s. A turbine flow meter was downstream of the vertical at a location specified by the manufacturer to attain accurate readings. This vertical leads to a tee junction where the flow is divided and then mixed back together in the upper plenum. A k-type thermocouple also sits at this tee junction to capture the temperature of the fluid before entering the test section with an uncertainty of ± 0.2ºC. The upper plenum was designed to mix and condition the flow using a series of screens and honeycombs as outlined for low-speed wind tunnels from Mehta and Bradshaw [56]. Honeycombs were made from PTFE and screens were made from stainless steel in order to avoid rust or corrosion with the working fluid, water. After the upper plenum, the flow passes through a reducer

where another honeycomb and screen allow for a fully developed inlet condition before entering the test section. The velocity of the inlet was verified between ports created at the top of the test section along the length. Once the flow goes through the test section, it is moved through a reducer before moving into the tank. This reducer helps to avoid exit affects and also mix the fluid within the tank before it gets fed back into the pump. The full experimental facility can be seen in Figure 2.8. Table 2.1 summarizes some of the key characteristics of the test section.

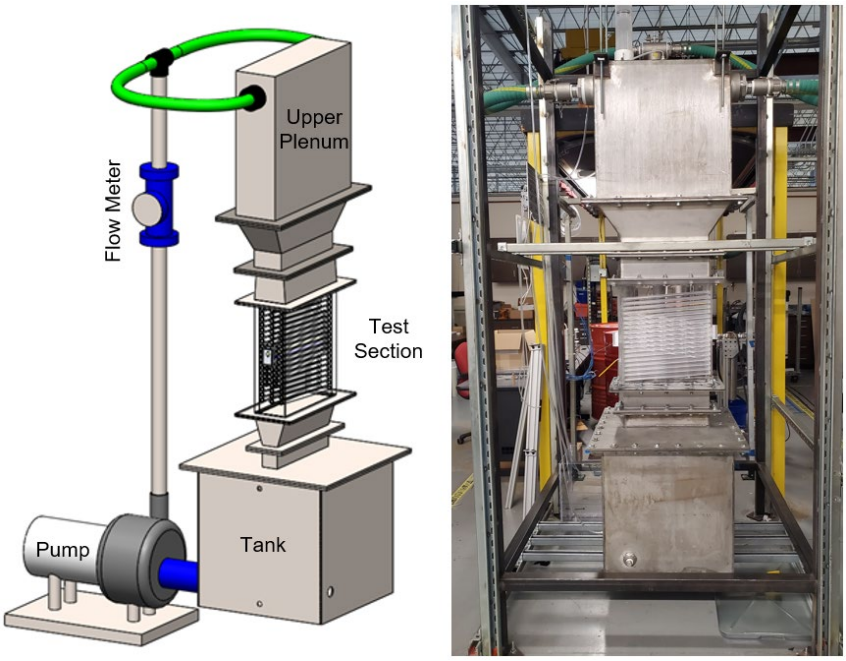

Figure 2.8 The vibration testing experimental facility

Table 2.1 Defining characteristics of the test section.

Characteristic	Value
Lateral pitch ratio, a	cyclical
Transverse pitch ratio, b	2.98
Number of rows	18, 9
Outer rod bundle angle	+ 4 degrees
Inner rod bundle angle	- 9 degrees
Tube (Rod) Material	Acrylic
Vibrating Tube (Rod) diameter, D_R	1.59 cm
Vibrating Tube (Rod) length, L_R	50.17 cm
Clearance diameter, D_C	2.09 cm
Spring Material	SS 316
Spring Rate, k	262.7 N/m

2.3. Experimental Data Acquisition

In order to capture the vibrational response of the rods from the outside of the module, a high-speed camera (Phantom Miro R311) was set-up on a rotational and vertical axis. Since the vibrating rods are at an angle, the camera is also mounted at an angle to capture the rod face normal to the image. Figure 2.9 shows the camera set-up beside the testing facility as well as a view of the enclosed and attached vibration module for a single rod vibrating case. The camera captured images of 768 × 768 pixels with the rod diameter covering about 80% of the image. Preliminary tests were conducted to compare the camera capture rate to the amount of motion visible from frame to frame, and a frame rate of 1,000 frames per second was chosen for the highest pixel displacement between frames to be ~ 20 pixels. An example of the camera image for the case with a single rod vibrating is shown in Figure 2.9.

Camera Set-up

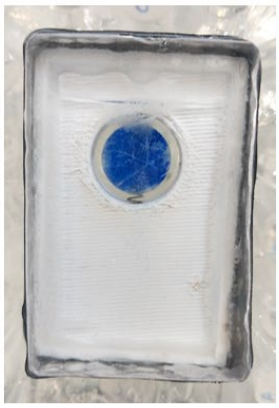

Attached Vibrating Module

Camera View

Figure 2.9 Experimental data was acquired using a high-speed camera focused on the rod/rods that were vibrating within the vibration module.

3. RESULTS

3.1. Image Analysis

Images were captured by the high-speed camera for each experimental condition at 1,000 frames per second for approximately 10 seconds. Larger images were taken to include at least one end of the module since the module was aligned with the test section prior to enclosure before reducing the image to a 768 × 768 pixel resolution for the single rod captures and 768 ×1024 pixel resolution for the adjacent rods' images. Images were rotated based on the alignment to the module. An example of an image from each configuration is shown in Figure 3.1.

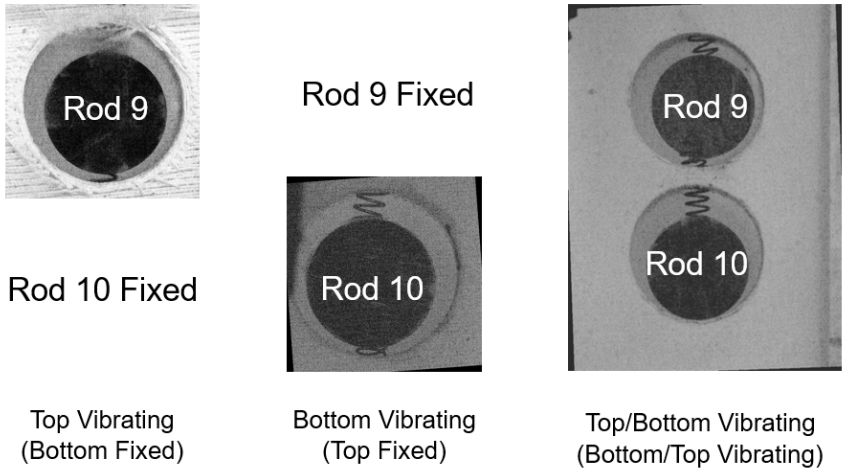

Figure 3.1 Camera images of each experimental configuration.

In order to analyze these images for their displacement and frequency of motion, an in-house code utilized the MATLAB built-in function "imfindcircles" to locate the centers of the circles when a range of diameter is provided using Hough Transform [57]. Processing of the images included changing the brightness and contrast, dividing the image into RBG color parts and iterating this process until the smoothest center location

output was realized for a set of images. An example of the sensitivity of the program to bright spots within an area that is supposed to be homogenous can be seen in Figure 3.2.

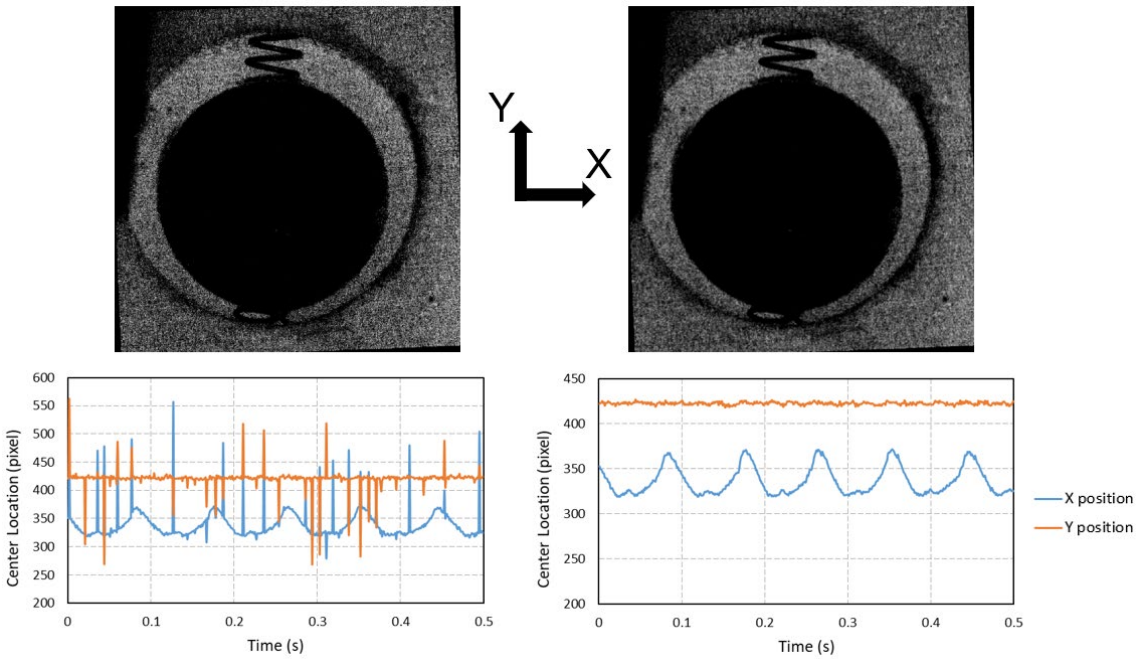

Figure 3.2 An example of the output from the circle center location tracking code that shows the sensitivity to changes in contrast within the circle area.

Depending on the clarity of the edge of the circle, there are times when no amount of image editing within reason would yield a clean center location, various filters were tested. In order to maintain any flow anomalies that might occur while getting rid of outliers, a moving average and standard deviation filter were applied. A moving average window of 40 data points and standard deviation limit of 5 was applied in these cases.

3.1.1. Pixel-to-MM Ratio and Uncertainty Calculation

For each experimental configuration, there is a specific ratio that converts the pixel to a specific length. This pixel-to-mm ratio is determined using the diameter of the rod and the diameter of the clearance, to get an average for the configuration. For each configuration, the rod and clearance have a particular diameter length in pixels, although this may vary as both are not perfect circles. Therefore, two lengths were taken, the diameter in x and diameter in y before averaging the two pixel-to-mm ratios.

It is important to take into consideration the tolerance of each when determining the uncertainty of the experimental results. The rod diameter, D_R, has a tolerance of ±0.026 cm and the clearance diameter, D_C, has a tolerance of ±0.038 cm. The pixel uncertainty based on the Hough Tracking method produces a pixel location to the one hundred thousandth. Nevertheless, this cannot be taken as the uncertainty since the program is in itself finding the center based on an average of edges found. The actual uncertainty for the pixel displacement is the uncertainty of the circle edge, or how blurry the circles edge is. For each experimental configuration, the uncertainty is not greater than 3 pixels.

Therefore, the maximum uncertainty for the mm to pixel ratio is 0.000213. A summary of the pixel-to-mm ratios and the average used to convert pixel motion to displacement in mm for each experimental configuration is shown in Table 3.1.

Table 3.1 Average pixel-to-mm ratio as a function of rod and clearance diameter

	pixel-to-mm ratio		
	Using D_R	**Using D_C**	**Average**
Top Vibrating (Bottom Fixed)	0.0332	0.0330	0.0331
Top Vibrating (Bottom Vibrating)	0.0550	0.0563	0.0557
Bottom Vibrating (Top Fixed)	0.0318	0.0322	0.0320
Bottom Vibrating (Top Vibrating)	0.0557	0.0557	0.0557

3.2. Results of Single vs. Adjacent Tube Vibration

In order to study the self- excited flow induced vibrational response relative to location, three configurations are studied at the same Reynolds number. From these three experimental configurations, the results are divided by: Top Vibrating (Bottom Fixed), Top Vibrating (Bottom Vibrating), Bottom Vibrating (Top Fixed), and Bottom Vibrating (Top Vibrating) as first mentioned in Table 3.1.

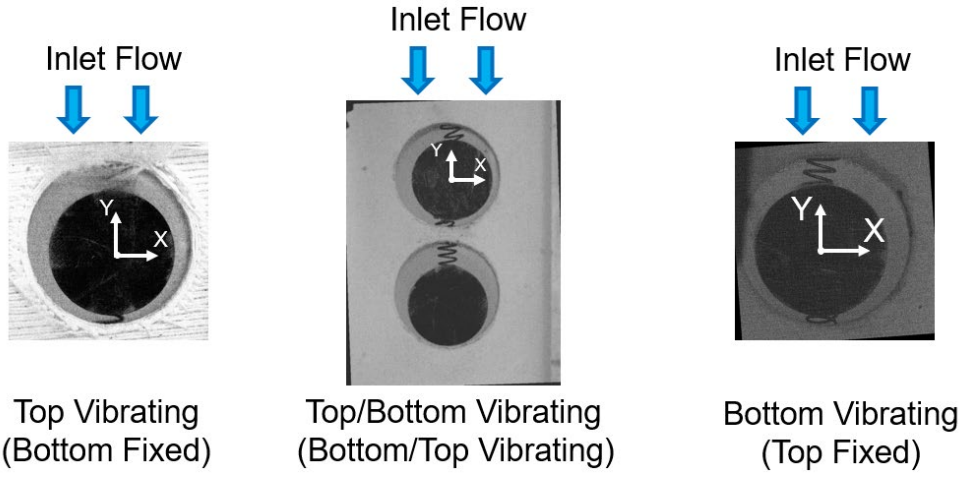

Figure 3.3 The three experimental configurations to study the single and adjacent tube vibration response.

For each configuration, the inlet velocity, V_∞, was 0.44 m/s which yields a Reynolds Number, Re_∞, of ~7,500 using the inlet velocity and rod diameter, D_R, as the characteristic length. Each set of tests took approximately 10 seconds of images at 1,000 frames per second. An example of a single image from each configuration is shown in Figure 3.3. From these frames it is clear that in some configurations, the rod did not sit in the center of the port during the starting position. This was due to the alignment issues between the angled rod and the spring ports. The location where the rods sit when there is no flow will be considered their neutral position and all analysis will consider this non-centered position the zero position from which displacement is considered.

3.2.1. Top Rod (Rod 9) Vibration Results

Results from the center tracking program divide the motion in the x- and y-directions. The motion for the Top Vibrating (Bottom Fixed) configuration is shown in Figure 3.4. From this figure there are various features that stand out. First, in the x-direction, there is a consistent frequency of motion at first glance that changes amplitude slowly over a period of about 2 seconds. In the y-direction, the frequency and amplitude of the motion is less consistent. There appears to be a pattern where the amplitude is ~ 5 pixels followed by ~ 15 pixels, consecutively, but there is not a consistency across the total time of data acquired.

Figure 3.5 shows the circle center motion in the x- and y- direction for the Top Vibrating (Bottom Vibrating) configuration. From these plots, there is a consistent

frequency and amplitude for the motion in both directions. There are the same patterns that were seen for the Top Vibrating (Bottom Fixed), such as the consecutive change in amplitude for the y-direction, but for this configuration it is consistent across the entire test period. Another visible agreement between the two cases is the constant frequency in the x- direction motion. While for the Top Vibrating (Bottom Fixed) case this constant frequency varies in amplitude along time, the Top Vibrating (Bottom Vibrating) case has a very consistent frequency and amplitude for the x-direction motion.

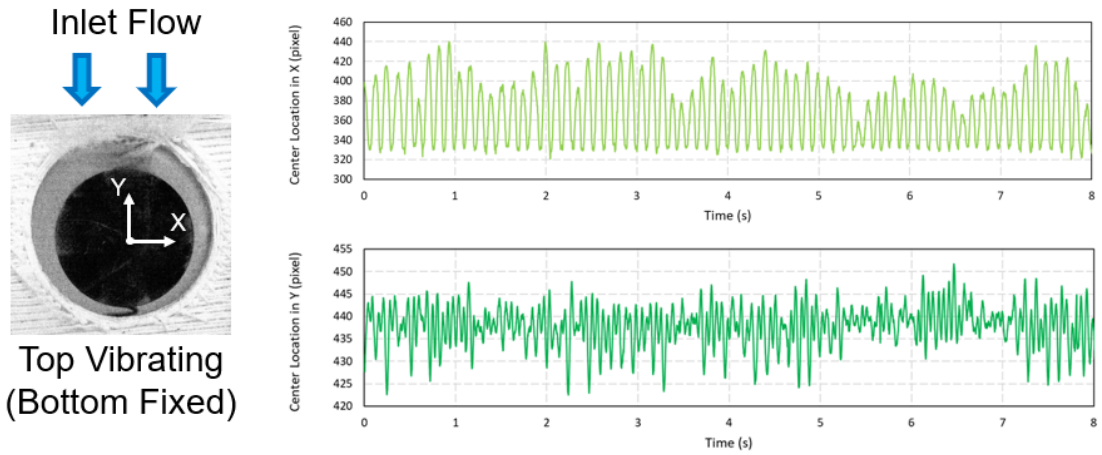

Figure 3.4 Center location plots for the x- and y-direction motion for the Top Vibrating (Bottom Vibrating) configuration at Re_∞ = 7,500.

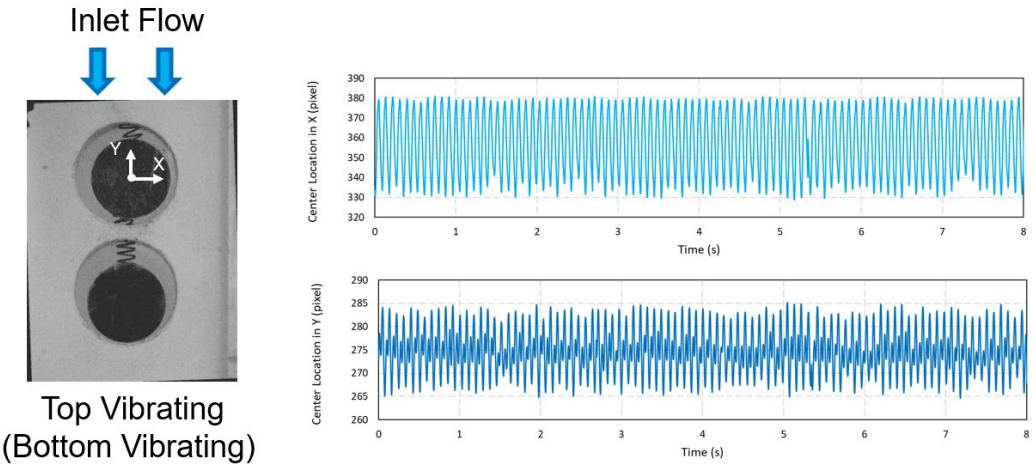

Figure 3.5 Center location plots for the x- and y-direction motion for the Top Vibrating (Bottom Fixed) configuration at Re_∞ = 7,500.

In order to better visually compare the amplitude and frequency of the motion, the displacement from the neutral position is calculated and then plotted in the same graph to compare the two configurations. Figure 3.6 does this for both the x- and y-direction displacements of both configurations and plots across a time window of 2 seconds.

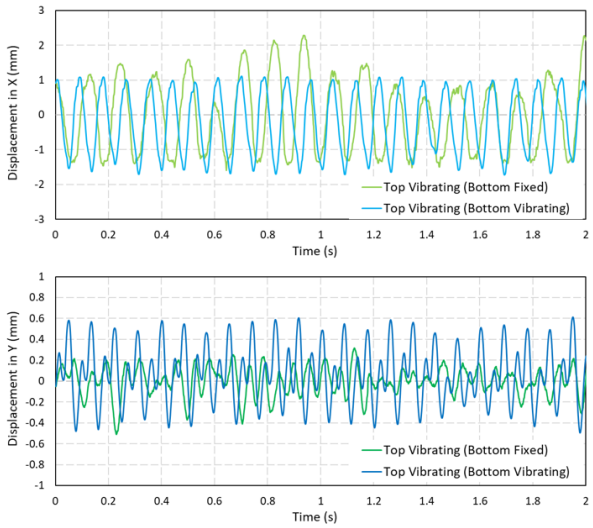

Figure 3.6 Comparison between the displacement in x- and y-directions in Rod 9, between the Top Vibrating (Bottom Fixed) and Top Vibrating (Bottom Vibrating) configurations.

From Figure 3.6, the frequency and amplitude of the vibration in the x- and y-direction are easily comparable. In the x-direction, the Top Vibrating (Bottom Fixed) configuration has a slower period than the Top Vibrating (Bottom Vibrating) case. In addition, the consistency of the frequency of both signals is clear but with the case of the Top Vibrating (Bottom Fixed) the major difference is the gradual change in amplitude. The y-direction displacement shows differences similar to that of the x-direction displacement in that Top Vibrating (Bottom Fixed) has a longer time for a single period and the signal is not well structured in that period. While for the Top Vibrating (Bottom Vibrating) case the displacement is consistent in frequency but during the time shown there is a period change in amplitude that becomes more evident.

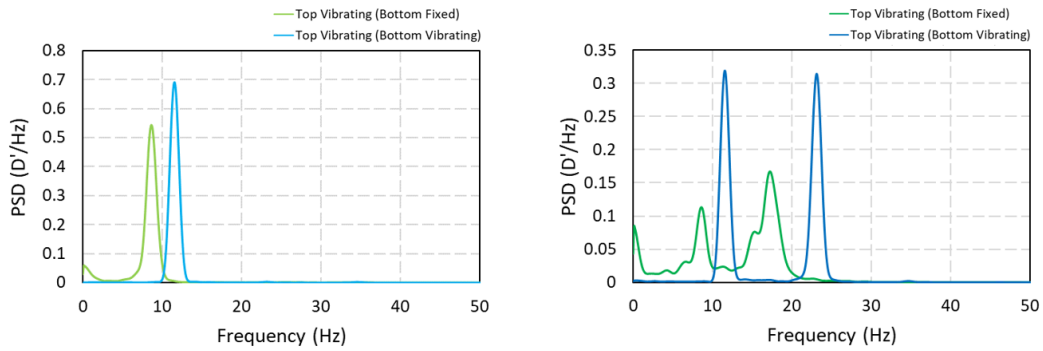

(a) **(b)**

Figure 3.7 PSD Plots for displacement between the Top Vibrating (Bottom Fixed) and Top Vibrating (Bottom Vibrating) in the (a) x-direction and (b) y-direction

One way to compare these oscillatory displacement plots is by computing a power spectral density function (PSD) function of the displacement. A PSD plot shows at which frequencies variations are strong. PSD functions were calculated using a Welch

function and used displacement intensity to amplify the variation. The function was calculated with a 20% integration window overlap and data plotted is limited to peaks with a 98% confidence level. Figure 3.7 shows the PSD plots for the four x- and y-displacement plots.

Table 3.2 Peak frequencies of PSD Plots from displacement between the Top Vibrating (Bottom Fixed) and Top Vibrating (Bottom Vibrating) in the x- and y-direction

	$f_{V,x}$ (Hz)	$f_{V,y1}$ (Hz)	$f_{V,y2}$ (Hz)
Top Vibrating (Bottom Fixed)	8.624	8.624	17.25
Top Vibrating (Bottom Vibrating)	11.56	11.56	23.12

From the PSD plots, the peak frequencies could be extracted and are presented in Table 3.2. From this table it can be seen that when Rod 9 (Top Rod) is allowed to vibrate on its own, Top Vibrating (Bottom Fixed), the frequency of vibration is 8.6 Hz. When two adjacent rods are allowed to vibrate, Top Vibrating (Bottom Vibrating), the frequency of vibration increases to 11.56 Hz. In the y-direction, both signals show the same frequency of vibration as the x-direction and the second peak is a multiple of the first.

3.2.2. Bottom Rod (Rod 10) Vibration Results

In similar manner to the analysis done with the top rod, the results for the center tracking program for the Bottom Vibrating (Top Fixed) configuration are presented in Figure 3.8. From the center motion, the x-direction shows some very unique patterns.

While the frequency of the motion looks consistent, there is a unique feature of this signal on the left side which looks like a "stall." This stall is a short move to the right, but then, return to left side, before fully moving to the right. At the right side, there is no similar feature, it is a sharp return to the left side. This is seen across the entirety of the center motion. Similar to the x-direction motion seen in Figure 3.4, Figure 3.8 also shows that there is a fluctuation in amplitude of motion in the x-direction. Similarly, looking at the y-direction motion, there is a less structured pattern. From the plot's y-axis, the range of motion is ~ 6 pixels while for the x-direction it is ~ 50 pixels.

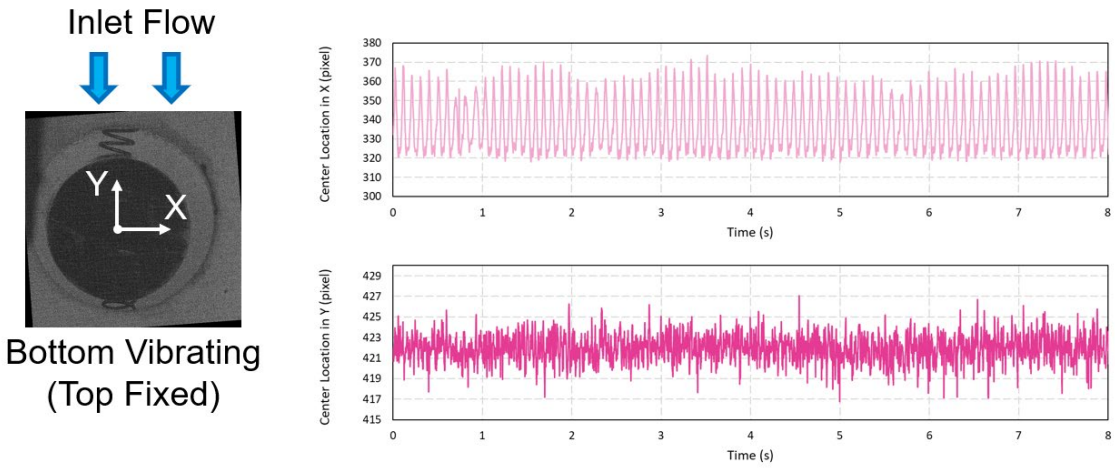

Figure 3.8 Center location plots for the x- and y-direction motion for the Bottom Vibrating (Top Fixed) configuration at Re_∞ = 7,500.

Figure 3.9 shows the same as Figure 3.8 for the Bottom Vibrating (Top Vibrating) configuration. From the x-direction center location plot, both the frequency and amplitude of the motion is very consistent across the entire test time. Unlike the

motion from the Bottom Vibrating (Top Fixed) configuration, there are no large fluctuations in amplitude or "stall" behavior seen. In the y-direction, the motion is similar to that seen in Figure 3.4 for the Top Vibrating (Bottom Vibrating) where the amplitude is consecutively changing.

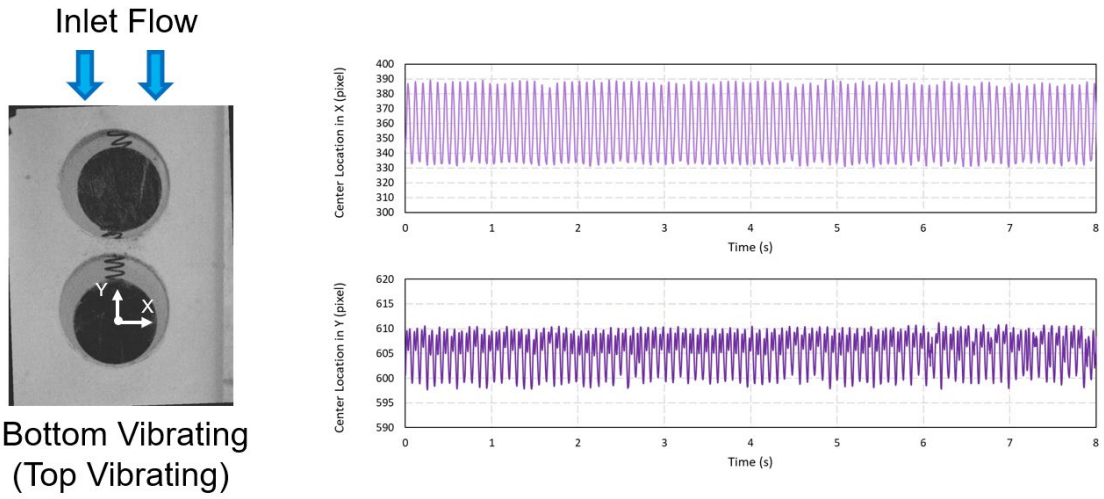

Figure 3.9 Center location plots for the x- and y-direction motion for the Bottom Vibrating (Top Vibrating) configuration at Re_∞ = 7,500.

A way to compare the two more clearly is by limiting the time scale to a shorter time period, 2 seconds, and normalizing both signals to their starting position. Figure 3.10 compares the x- and y- displacement between the Bottom Vibrating (Top Fixed) and Bottom Vibrating (Top Vibrating) configurations.

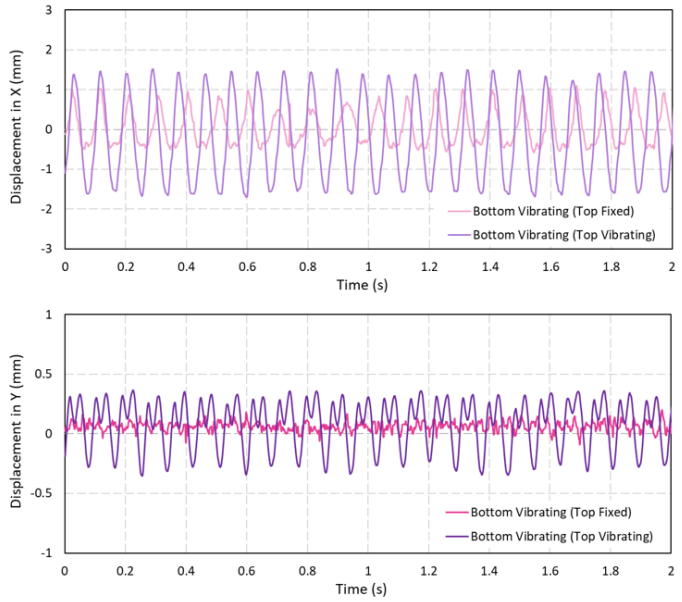

Figure 3.10 Comparison between the displacement in x- and y-directions in Rod 10, between the Bottom Vibrating (Top Fixed) and Bottom Vibrating (Top Vibrating) configurations.

From Figure 3.10, the displacement in both configurations for Bottom Rod, Rod 10, is much more different than the displacement comparison seen for the Top Rod, Rod 9. Focusing on the x-direction displacement, the amplitude and frequency in the positive x-direction is very similar between the two configurations. While the "stall" seen in the Bottom Vibrating (Top Fixed) configuration reduces the amplitude of the displacement in the negative x-direction, there is a slight "stall" also seen in the negative x-direction displacement from the Bottom Vibrating (Top Vibrating) case. Therefore, showing that

this behavior is characteristic of the tube bundle. From the displacement in the y-direction plot, it is clear that there is almost no motion from the Bottom Vibrating (Top Fixed) case, while for the Bottom Vibrating (Top Vibrating), the pattern seen in the Top Vibrating (Bottom Vibrating) case is seen here as well.

Similar to the Top Vibrating configurations, the PSD plots were computed and are shown in Figure 3.11. The PSD function was also computed using a displacement intensity with a 10% and 20% signal overlap, for the Bottom Vibrating (Top Fixed) and Bottom Vibrating (Top Vibrating), respectively and limiting peaks to those with 98% confidence level.

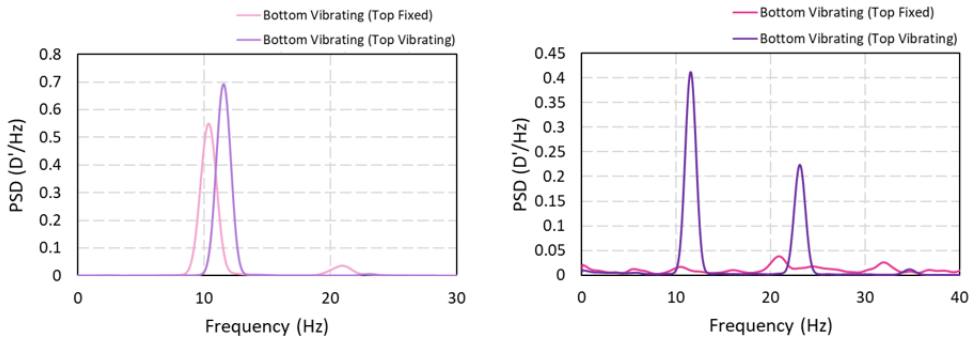

(a) **(b)**

Figure 3.11 PSD Plots for displacement between the Bottom Vibrating (Top Fixed) and Bottom Vibrating (Top Vibrating) in the (a) x-direction and (b) y-direction

Table 3.3 Peak frequencies of PSD Plots from displacement between the Bottom Vibrating (Top Fixed) and Bottom Vibrating (Top Vibrating) in the x- and y-direction

	$f_{V,x}$ (Hz)	$f_{V,y1}$ (Hz)	$f_{V,y2}$ (Hz)
Bottom Vibrating (Top Fixed)	10.28	20.84	--
Bottom Vibrating (Top Vibrating)	11.59	11.59	23.17

Figure 3.11, along with the peak frequency values in Table 3.3, show the significant frequencies of the displacement plots for the Bottom Vibrating (Top Fixed) and Bottom Vibrating (Top Vibrating) cases. As was seen in Figure 3.10, the frequency of the two cases in the x-direction are similar with a difference between the two of ~ 1.31 Hz. Compared to the difference between the two Rod 9 cases, which had a difference of ~ 3.14 Hz, the addition of an adjacent vibrating tube appears to affect the upstream tube more. As was seen in the two configurations of Rod 9, the significant frequencies of displacement are the same in the x-direction and in the y- direction for the Bottom Vibrating (Top Vibrating) case as well. Due to the lack of displacement in the y-direction for the Bottom Vibrating (Top Fixed) case, there were no significant peaks produced.

3.2.3. X vs Y Plots

Another way that the displacement of the rods can be visually compared is with X vs Y plots for each configuration. Figure 3.12 shows each configuration beside its physical location plot. Using the neutral or zero position of the circle as (0,0) of the plot, the shape of the motion between configurations is distinctively different. The location of the neutral position plays an important role to the motion, such as with the Bottom Vibrating (Top Vibrating) case. In this case, the rod sits at the base of the clearance and therefore, the shape of the motion is limited.

The Top Vibrating (Bottom Vibrating) shape has a very particular and consistent smooth figure eight shape, while the Top Vibrating (Bottom Fixed) shape is very

choppy, which could mean an issue with the spring, and curves in the opposite direction with a very consistent pattern on the left but occasionally goes much farther to the right.

Similar to the smooth pattern discussed for its adjacent rod, the Bottom Vibrating (Top Vibrating) case also shows a very smooth and structured movement of the rod. Unfortunately, we know this is due to the neutral position sitting the rod so low. Nevertheless, while the motion is split evenly between the positive and negative x-direction, the Bottom Vibrating (Top Fixed) case shows a much stronger push to the right, than the left.

Overall, there are clear differences in the vibrational response paths of each case and it is suggested by the experimental results that the addition of an adjacent vibrating tube changes the path, frequency and amplitude of both the tubes.

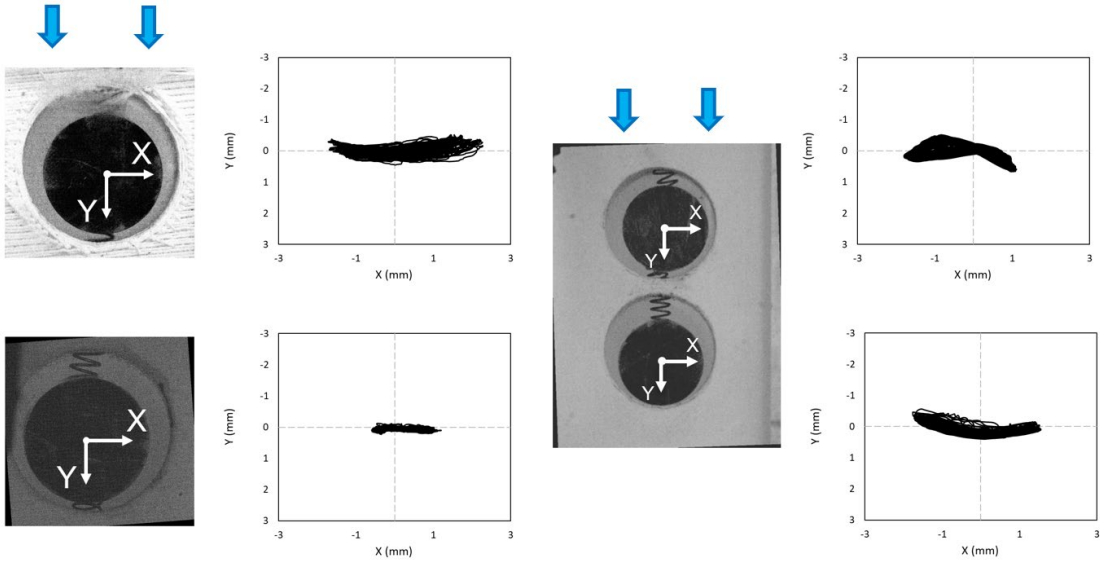

Figure 3.12 X vs Y plots comparing the vibrational response for each tube configuration at Re_∞ = 7,500 capturing ~ 10 seconds of experimental data for each

3.3. Results of Increasing Reynolds Number

Another way to analyze the behavior of the self-excited flow induced vibration is to study the effect of Reynold's number on the vibration of the tube. Experiments looked at the same configuration at interval Reynold's number increments after the pump was allowed to settle at the specific inlet flow rate. Using the Bottom Vibrating (Top Fixed) configuration, the inlet velocity was increased from 0.22 m/s to 0.49 m/s corresponding to Re_∞ from 3,800 to 8,300. Images were taken at 1,000 fps for approximately 4 seconds and were analyzed as described in Section 3.1 – 3.2.

Results for the x-direction centroid location are presented in Figure 3.13. From these plots, there is a clear difference that occurs in the motion between Re_∞ = 4,700 and 5,600. While at Re_∞ = 3,800 the motion barely resembles a steady motion, by Re_∞ = 5,600 the pattern of motion is well established and features such as the "stall" seen

previously in Section 3.2 are visible. Another feature that can be seen in Figure 3.13 is the occasional change in amplitude behavior as the Re_∞ increases. For Re_∞ = 5,600 the amplitude of the motion in both the positive and negative x-direction is very consistent. This does not appear in the consecutive tests, for example, for Re_∞ = 7,500 the plot shows a clear change in period and amplitude between the 0.6 to 1.0 seconds from the surrounding data.

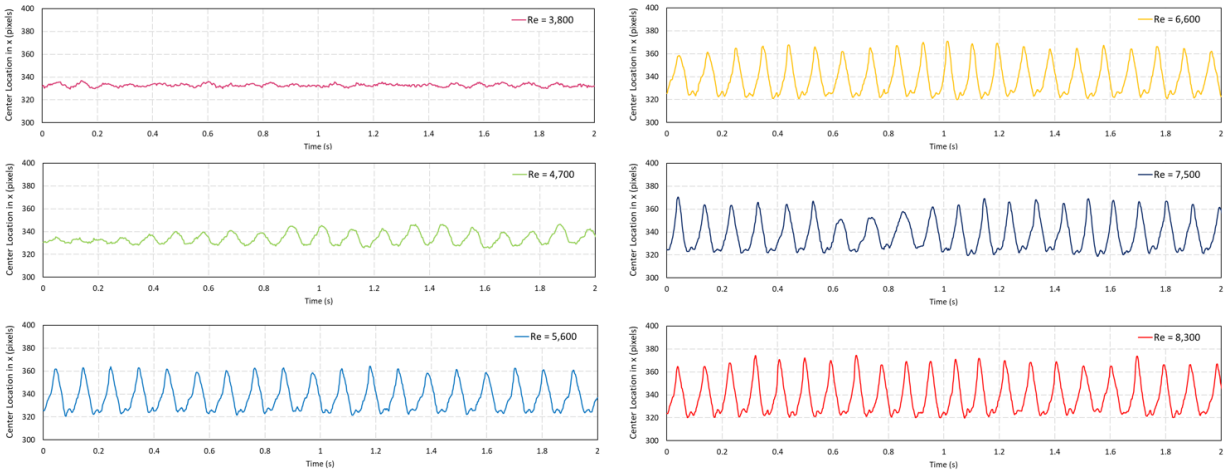

Figure 3.13 X-direction center location plots for the Bottom Vibrating (Top Fixed) configuration from Re_∞ = 3,800 to 8,300.

In order to compare the signals to each other more clearly, Figure 3.14 overlaps the motion in the x-direction for each Re_∞ as a displacement from the neutral position. Some clear features of the motion are also shown as independent of Re_∞ after a certain flow rate, such as the "stall" on the negative x-direction. At Re_∞ = 4,700, there is a clear development of this feature that stays consistent as Re_∞ increases. In the positive x-direction, the end of the motion is sharp and differences in amplitude are more evident in

this figure. Figure 3.14 also clearly shows how the frequency of motion occasionally aligns between increasing Reynold's numbers.

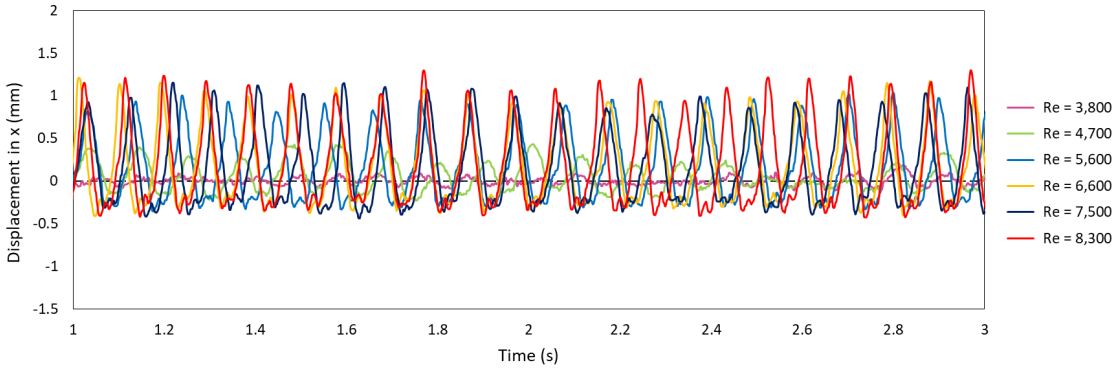

Figure 3.14 Displacement in the x-direction for Bottom Vibrating (Top Fixed) configuration from Re_∞ = 3,800 to 8,300

Features such as this can be further seen when converting the data into a PSD plot. Similar to previous results, the PSD function was created using a welch function to plot the displacement intensity with a 30% signal overlap and limited the peaks to those with 98% confidence level. In order to compare the dominant frequencies, Figure 3.15 shows the PSD signal for each Re_∞. Table 3.4 compares the values of the highest peak for each Re_∞ set of x-direction displacements. From the table, the signals for Re_∞ = 3,800, 6,600 and 7,500 all have the predominant frequency of motion at 10.28 Hz. The farthest frequency of motion from this is at Re_∞ = 4,700 with a peak frequency at 9.17 Hz.

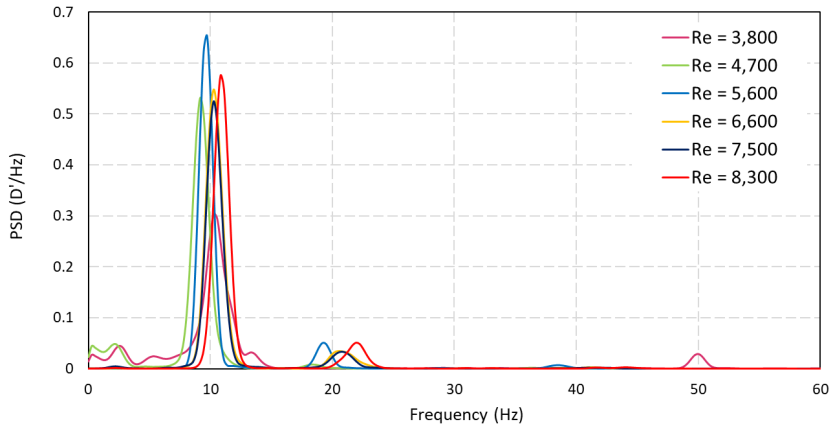

Figure 3.15 PSD signals for the x-direction displacement for the Bottom Vibrating (Top Fixed) configuration for Re_∞ = 3,800 to 8,300

Table 3.4 Peak frequencies of PSD Plots from displacement the Bottom Vibrating (Top Fixed) in the x-direction for Re_∞ = 3,800 to 8,300

Re_∞	Freq (Hz)	PSD (D'/Hz)
3,800	10.2835	0.3037
4,700	9.1718	0.5318
5,600	9.7276	0.6534
6,600	10.2835	0.5483
7,500	10.2835	0.5250
8,300	10.8394	0.5756

Similarly, the y-direction motion was plotted as a function of Reynolds number, Re_∞ in Figure 3.16 where each Re_∞ has an individual plot. While the x-direction motion is defined by displacement ranging from 30 to 40 pixels, the y-direction motion at the highest Re_∞ has a maximum displacement of 5 pixels. This result is expected, as seen previously, due to the springs sitting in the y-direction. As seen in the motion for the x-direction, the y-direction motion also sees a significant difference between Re_∞ = 4,700 and 5,600. After Re_∞ = 5,600 the amplitude of the y-direction motion stays consistently at ~ 4 pixels. One unique feature that is noted in Figure 3.16 but is more evident in

Figure 3.17 is the center of the motion for the rod. In order to calculate the displacement from the pixel motion, a starting or neutral position was taken before each test. Looking at Figures 3.16 and 3.17, it is clear that this center changes from test to test. In order to normalize and compare the displacement, the centers of each test had to be determined. Table 3.5 shows how the center for each test shows a consistent x-direction center but a changing y-direction center. This suggests that the flow rate for each specific test had an effect that raised Rod 10 more than 4 pixels between Re_∞ = 3,800 and 8,300. Since the vibration of the rod is within this order, the movement in center location between tests is significant.

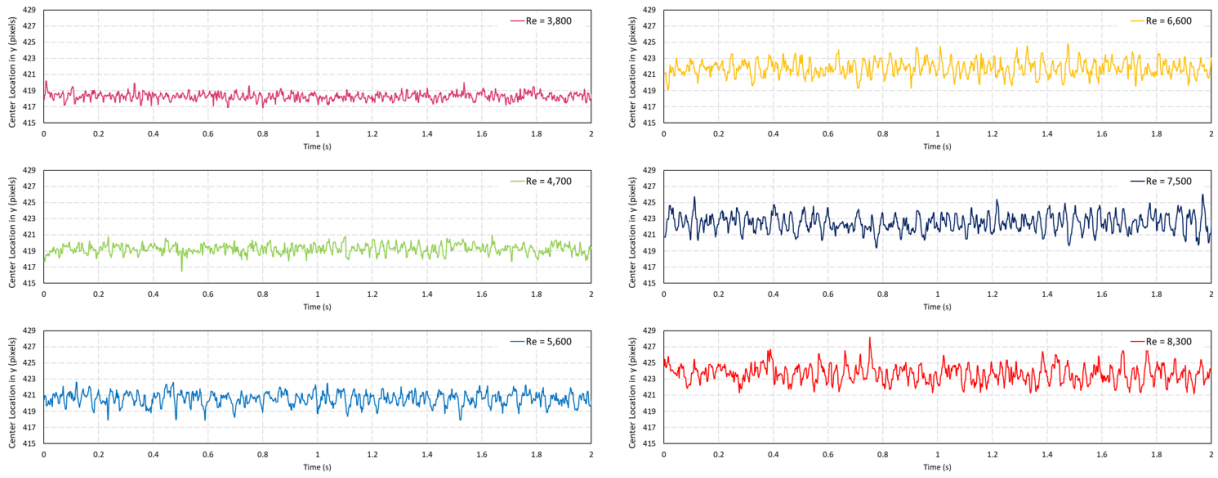

Figure 3.16 Y-direction center location plots for the Bottom Vibrating (Top Fixed) configuration from Re_∞ = 3,800 to 8,300.

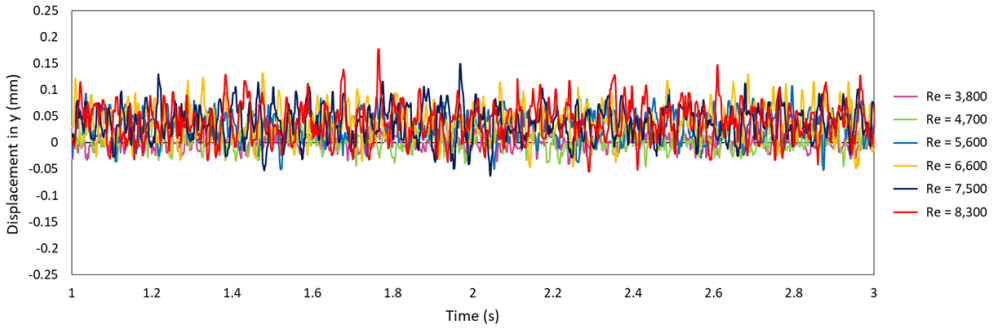

Figure 3.17 Displacement in the y-direction for Bottom Vibrating (Top Fixed) configuration from Re_∞ = 3,800 to 8,300

Table 3.5 Starting/ Neutral center location in pixels for each Reynold's number test

	Center location	
Re_∞	X	Y
3,800	332.75	418.27
4,700	332.75	419.07
5,600	332.76	419.54
6,600	332.77	420.64
7,500	332.75	421.33
8,300	332.74	422.33

Comparing the signals using their PSD plots gave some better insight into the trends that were occurring within the y-direction vibration. From Figure 3.18, the density of the function was not as clearly defined with single peaks as was seen in Figure 3.15. From the figure, it is clear that the y-direction motion has some significant peaks around 20 Hz for each Re_∞. From the signal itself, as given in Table 3.6, these peaks do not have a density higher than 0.25 D′/Hz. This peak with a density of 0.2375 D′/Hz is at 19.455 Hz for Re_∞ = 5,600. Looking back at the peak frequencies for the x-direction displacement, Re_∞ = 5,600 has a significant peak at 9.7276 Hz which is half the 19.455 peak found here. The peaks of the remaining Re_∞ are also approximately twice the

significant peak of the x-direction displacement. Table 3.6 also clearly shows how Re_∞ = 3,800 and 7,500, and Re_∞ = 4,700 and 8,300 have the same significant peak at 20.845 and 21.956, respectively.

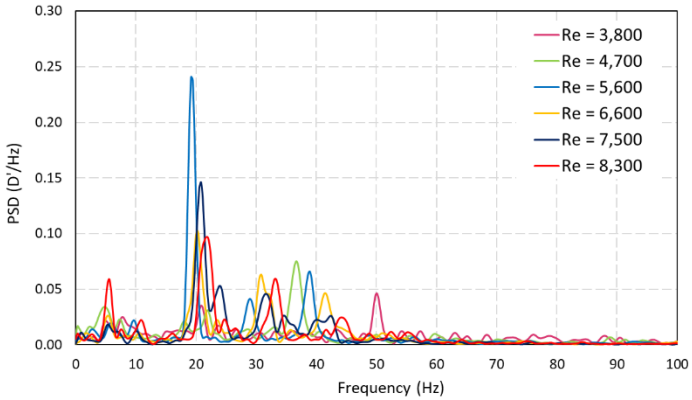

Figure 3.18 PSD signals for the y-direction displacement for the Bottom Vibrating (Top Fixed) configuration for Re_∞ 3,800 to 8,300

Table 3.6 Peak frequencies of PSD Plots from displacement the Bottom Vibrating (Top Fixed) in the y-direction for Re_∞ 3,800 to 8,300

Re_∞	Freq (Hz)	PSD (D'/Hz)
3,800	20.845	0.0354
4,700	21.956	0.0311
5,600	19.455	0.2375
6,600	20.289	0.1024
7,500	20.845	0.1462
8,300	21.956	0.0967

To get a visual representation of the effect that the Reynolds number, Re_∞, had on the flow-induced vibration of Rod 10 in the Bottom Vibrating (Top Fixed) configuration, Figure 3.19 presents the X vs Y plot of the rod center for each Re_∞. From the figure, there are clear patterns to the effect of increasing Re_∞. Before Re_∞ = 5,600 the motion is very localized and no preference of side or shape is clear. At Re_∞ = 5,600, the shape of

the motion is defined by a short downward movement to the left and a longer less downward inclined movement to the right. As Re_∞ increases, the left side appears consistent while the right-side movement extends further to the right. On either the left or right side, the rod is being pushed downward from its center location.

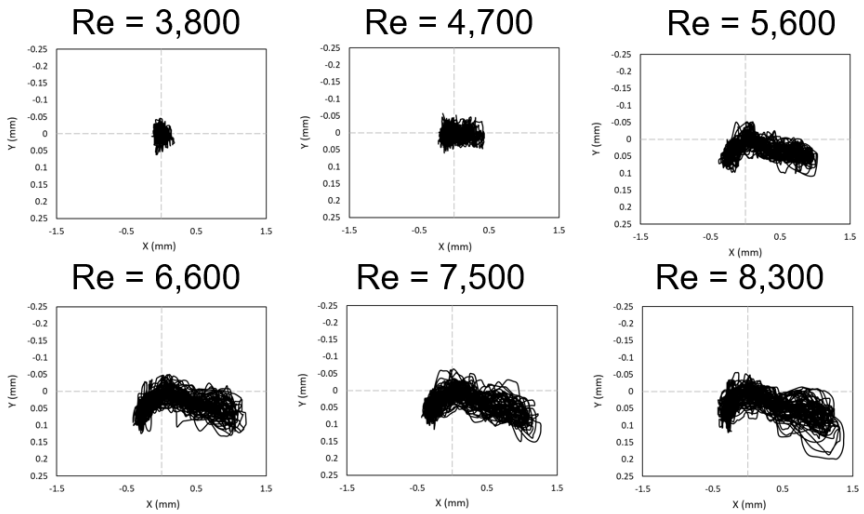

Figure 3.19 X vs Y plots comparing the vibrational response for the Bottom Vibrating (Top Fixed) configuration from Re_∞ = 3,800 to 8,300

3.4. Experimental Natural Frequency, f_N

As discussed in Section 1.1, the natural frequency of the system is an important characteristic to the correlations of flow characteristics and limitations of vibration. This natural frequency can be calculated or it can be experimentally determined. The natural frequency can be determined by either allowing the system to settle and taking the peak frequency of the motion or twice the number of cycles within a 0.5 second period. Given the experimental nature of this study, a test facility was created to determine the natural frequency of the spring-module system.

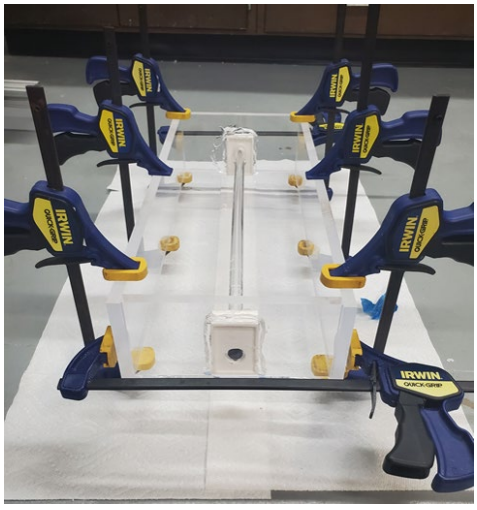

Figure 3.20 Experimental Set-up to determine the natural frequency, f_N, of the system

In order to experimentally determine the natural frequency, the test section shown in Figure 3.20 was created. The module was set up to sit in a still bath of the working fluid of the system, water. Similar to the experiments discussed previously, a high-speed camera was set-up to capture the motion of the rod from a position at the maximum displacement in the x-direction. The camera sat facing the rod directly and Figure 3.21 shows an example of the image captured at the start of the test. For this experiment images were captured at 2,000 fps in order to reduce the amount of pixel motion between frames.

Analysis was conducted similarly, aligning the image using the module and then using the Hough Transform tracking function within MATLAB to capture the center of the circle. Figure 3.22 shows the center location of the rod in the x-direction for 0.5 seconds. From this image there is approximately 3.5 cycles of motion before the rod settles. This agrees with the results of the PSD function that showed the most significant

peak at 7.01 Hz. Therefore, the natural frequency determined experimentally of the rod within the module, or the system, is ~ 7.0 Hz.

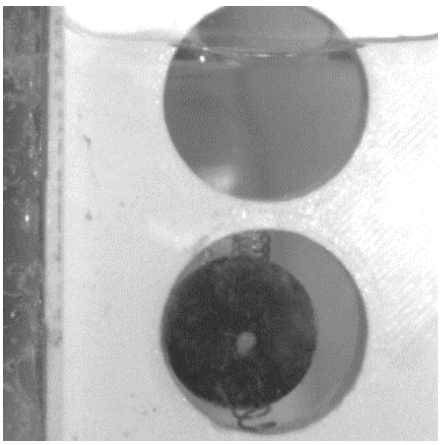

Figure 3.21 Example image from set taken to determine the natural frequency, f_N, of the system

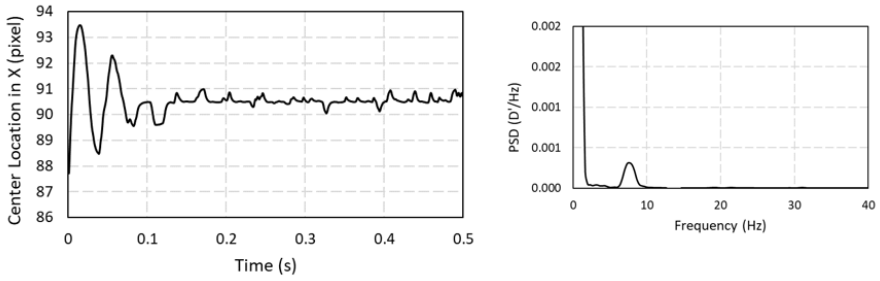

Figure 3.22 Settling time plot and PSD function to determine the natural frequency, f_N, of the system

4. DISCUSSION

4.1. Flow Physics of Tube Vibration

4.1.1. The Addition of an Upstream or Downstream Vibrating Rod

When looking at the motion from the experiments conducted in this study, it is known that the regions above and below the tubes are where eddys turn into vortices [11, 13, 14, 15, 16, 17, 18]. When these vortices grow large enough, they get pulled into the streamline flow, therefore pushing the tube away from the vortex entering the streamline. This vortex shedding phenomena is well understood for uniform tube bundles. In helical coil tube bundles, this vortex shedding switches sides continuously, a flow characteristic seen previously by the research team at Texas A&M University [6].

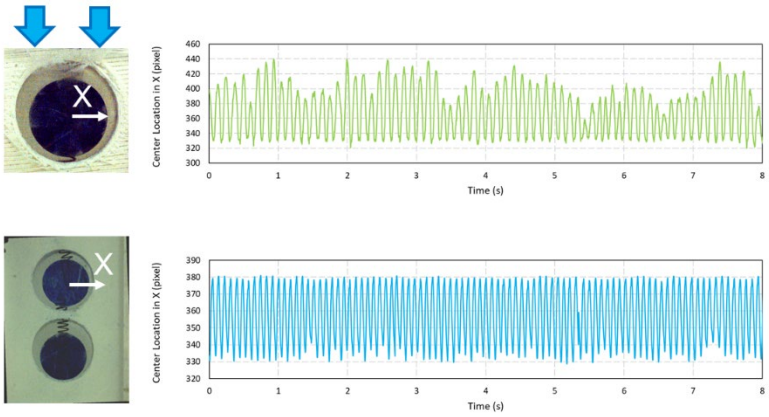

Figure 4.1 X-direction center location pixel motion for Top Vibrating (Bottom Fixed) and Top Vibrating (Bottom Vibrating) configurations

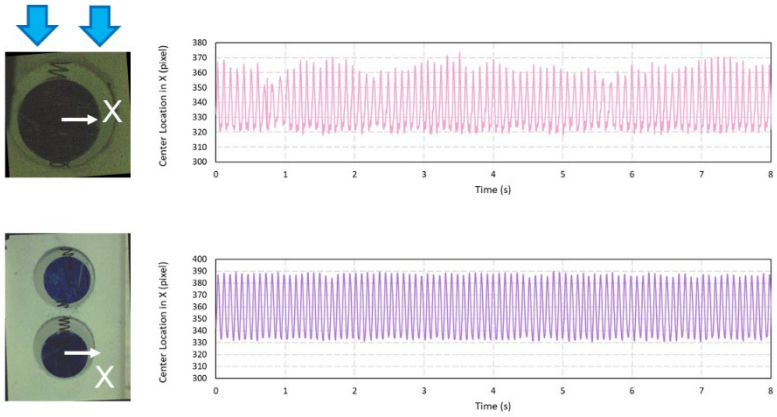

Figure 4.2 X-direction center location pixel motion for Bottom Vibrating (Top Fixed) and Bottom Vibrating (Top Vibrating) configurations

Results presented in Section 3.2 showed that there were differences between the self-induced vibration response between a single rod vibrating and its response when the rod adjacent to it was also allowed to vibrate. First, examining the behavior of the x-direction vibration response of the Top Vibrating (Bottom Fixed) configuration at Re_∞ = 7,500 to that of the corresponding configuration Top Vibrating (Bottom Vibrating) in Figure 4.1 shows the differences in amplitude and period frequency. The vibration in the Top Vibrating (Bottom Fixed) motion is defined by a precise displacement to the left, negative x-direction, and changing amplitude to the right, positive x-direction. While at first there was speculation as to if this effect is created by the spring catching onto an end of the module, the modules were changed to test this and the following sets of experiments supported that this was not the case. The same precise displacement to the left side is seen from the Bottom Vibrating (Top Fixed) configuration in Figure 4.2. This suggests that the vortex shedding behavior on the right of the tube is more uniformly

applying force onto the rod than the left side. On the left side of the rod, the vortex shedding behavior appears to fluctuate in intensity, creating the constantly changing amplitude in the positive x-direction from 360 to 440 pixels. When the rod downstream or upstream of the single rod is also allowed to vibrate, this behavior switches sides. Figure 4.1 shows how the center location in the x-direction of the Top Vibrating (Bottom Vibrating) configuration becomes very consistent, reaching 380 pixels location every time across the 8 seconds of data, but on the left, or negative x-direction, the center location moves between 330 and 340 pixels. In Figure 4.2, there is little to no fluctuation on either side of the motion captured by the Bottom Vibrating (Top Vibrating) configuration.

While the majority of flow-induced vibration studies on tube bundles focus on a single tube response, a study by Lin and Yu in 2005 [32] also looked at the effect of an adjacent tube vibrating and showed that upstream cylinders have a significant influence on the amplitude response of the monitored cylinder. The study found that downstream cylinders could suppress the vibration amplitude of the monitored cylinder. In this study, the same is observed. From the addition of a downstream rod, Figure 4.1 shows the decrease of pixel motion from ~120 pixels to ~50. Figure 4.2 shows the addition of an upstream rod and the maximum difference of vibration amplitude is ~ 30 pixels.

In terms of vibration frequency, f_V, the values from the PSD functions also show the influence that the addition of a downstream or upstream vibrating rod has on the rod studied. Table 4.1 shows the peak frequencies for the displacements shown in Figure 4.1 and 4.2. Between the addition of a downstream rod vibrating, the frequency for Rod 9

vibration frequency increased 2.94 Hz. When an upstream rod was allowed to vibrate above Rod 10, the vibration frequency increased 1.31 Hz. From this study it can be seen that the addition of an upstream or downstream tube affects the tube's vibration response in this particular tube bundle geometry.

Table 4.1 Vibration frequency amplitudes for the x-direction motion of Rod 9 &10

	f_V
Top Vibrating (Bottom Fixed)	8.62
Top Vibrating (Bottom Vibrating)	11.56
Bottom Vibrating (Top Fixed)	10.28
Bottom Vibrating (Top Vibrating)	11.59

4.1.2. The effect of increasing Reynolds Number

In the second part of this study, the effect of Reynolds Number was studied by increasing the inlet flow rate incrementally from 0.22 m/s to 0.49 m/s corresponding to Re_∞ = 3,800 to 8,300 for the Bottom Vibrating (Top Fixed) configuration where Rod 10 is the only rod vibrating within the system. Figure 4.3 shows three of the X vs Y plots on the same coordinates in order to see the difference in area where the center of the rod moved. At the lowest Re_∞ = 3,800, the rod's center remains within a narrow area. From the figure, the maximum displacement it has is ~ 0.07 mm in the y-direction and ~ 0.25 mm in the x-direction. At Re_∞ = 5,600, the shape and magnitude of the motion has become a downward V-shape with the right side having much larger displacement than the left. From Re_∞ = 5,600 until Re_∞ = 8,300, the shape of the motion remains the same and the displacement, or amplitude of motion, increases between each Re_∞. The consistent shape of the motion after Re_∞ = 5,600 describes a consistent flow behavior

surrounding the rod. The change in amplitude suggests a change in the size of the surrounding flow structures, the vortices, which can move the rod farther in either direction when shedding occurs. The shape of the motion therefore suggests that the vortices that shed on the left of the rod are larger than that of the ones shedding on the right. While the spring is trying to maintain the rod in the center, the force of the vortex shedding will push the rod to either side depending on the streamline the vortex is shedding into. Figure 4.3 shows that there is a certain flow rate at which this shape forms and the surrounding flow is consistent regardless of the Re_∞ within the experimental limits.

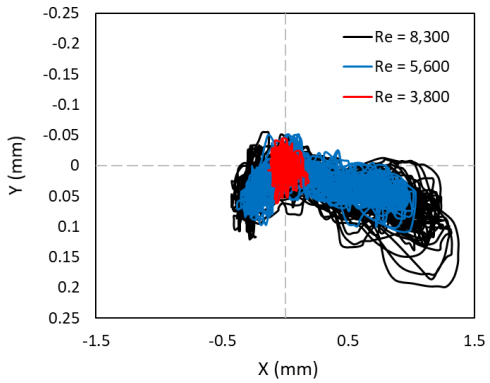

Figure 4.3 X vs Y plots for three different Re_∞ for the Bottom Vibrating (Top Fixed) configuration

Previous studies that track tube vibration have conducted this shape analysis as modes of vibration. A mode of vibration is a pattern of vibration defined by several points with different amplitudes of deflection. As seen from Figure 4.3, the vibration pattern can be described by two dimensions, a radius and angle. Converting Figure 4.3 to polar coordinates where (0,0) in the cartesian coordinates is the reference point, and x-axis in the positive direction is the reference direction, the shape can be defined with a

radius and angle for each cycle of motion. Figure 4.4 shows an example of the data from Figure 4.3 for Re_∞ = 5,600 with the polar coordinates overlaid. From this data, the radius and angle of the motion can define the mode 2 shape of the center displacement. The shape can be divided into two different curves, the right side, r_1, and the left side, r_2, displacement radii. To get a statistical average of the end data, all inflection points in the x-direction were used as end points for the curves and averaged. The corresponding y-direction centers were also averaged to determine the end points for r_1 and r_2. These coordinates in x- and y- direction were also used to determine the internal angle and subsequent polar coordinate angles were calculated. The results for the mode number 2 shapes defined by the radii and angle are presented in Table 4.2 for each Re_∞.

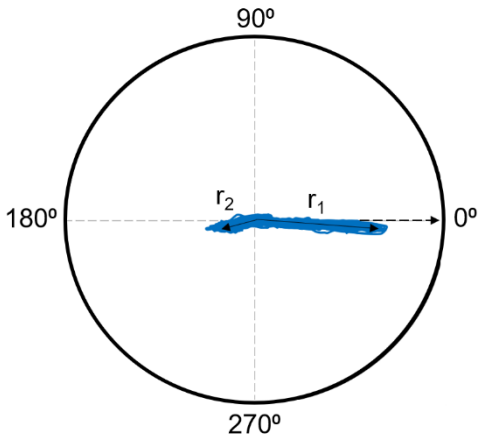

Figure 4.4 Polar coordinate plot for the mode 2 displacement from the X vs Y plot

Table 4.2 Mode 2 shapes defined by their radii and angles for the displacement of the rod for each Re_∞ where the motion has a defined shape

Re_∞	r_1 (mm)	θ_1 (deg)	r_2 (mm)	θ_2 (deg)
5,600	0.83	356.23	0.24	197.29
6,600	0.92	355.25	0.30	197.51
7,500	1.07	355.00	0.35	192.71
8,300	1.10	355.26	0.37	192.97

Examining the results from Table 4.2 shows that there is consistency in the angle of the motion of the right-side vibration, all at ~ 355 degrees and the left side changes ~ 5 degrees between Re_∞ = 6,600 and 7,500. Nevertheless, there is a clear correlation between the radius lengths, r_1 and r_2, to the Re_∞.

The results from the PSD plots for the vibration in the x- and y- directions is shown in Table 4.3. While there is a specific Re_∞ where the shape of the vibration is set, from Table 4.3 there is no specific point at which the Re_∞ changes vibration frequency. From Re_∞ = 3,800 to 8,300 the vibration frequency in the x-direction varies 1.67 Hz and, in the y-direction varies 2.51 Hz. The correlation between amplitude of vibration with Reynolds number and independence of frequency of vibration from Reynolds number is an expected characteristic of tube bundles.

Table 4.3 Dominant peak frequency of vibration in both the x- and y-direction for each Re_∞

Re_∞	f_V in x (Hz)	f_V in y (Hz)
3,800	10.2835	20.845
4,700	9.1718	21.956
5,600	9.7276	19.455
6,600	10.2835	20.289
7,500	10.2835	20.845
8,300	10.8394	21.956

4.2. Vortex Shedding and Strouhal Number Comparison

One way that the dominant peak frequencies of displacement are compared is by determining the Strouhal number as introduced in Section 1.1. Strouhal Number is a nondimensional parameter that represents the oscillations of the flow due to inertial forces compared to changes in velocity due to the convective acceleration of the flow. Using the experimental results for the peak frequencies as f_v, the vortex shedding frequency, the remaining characteristic in the equation is the gap velocity, V_g. For most tube bundle geometries, the calculation of gap velocity is straight forward. There are equations for staggered and in-line tube bundles, shown in Equations 4.1 and 4.2. Nevertheless, due to the changing geometry of the bundle, there are locations along the test section when the tube bundle of this study is inline and locations it is staggered.

$$V_{g,\ staggered} = \frac{S_T}{2\left(\sqrt{S_T^2+S_L^2}-D\right)} V_\infty \qquad \text{Eq 4.1}$$

$$V_{g,\ inline} = \frac{S_T}{(S_T-D)} V_\infty \qquad \text{Eq 4.2}$$

Table 4.4 Gap velocity for the tube bundle as an in-line and staggered tube bundle

	V_g (m/s)
Inline	0.663
Staggered	0.742

To be able to compare the changing geometry of the tube bundle of this study, the inline and staggered gap velocities were calculated and will be utilized as the expected range of gap velocity. Using these as the limits to the gap velocity, Strouhal number, St, can be calculated using the general equation given in Eq 1.3. for each

configuration using the dominant peak frequency as the vortex shedding frequency. Table 4.5 shows the frequency used as the vortex shedding frequency and the corresponding Strouhal number if the bundle were considered inline and staggered. Tube bundles are generally known to have St ~ 0.2 for a stable system, meaning that the oscillations inertial forces are approximately 20% of the convective acceleration the flow is under [12]. Table 4.5 shows that when this tube bundle is inline or staggered, the Strouhal number ranges from 0.1 to 0.19. While a system is generally known to have a single vortex shedding peak frequency, because the changes in configuration cause a change in the vortex shedding frequency, adding an upstream or downstream vibrating rod can change the Strouhal number up to 4%.

Table 4.5 Strouhal Number calculation for each configuration as an inline or staggered tube arrangement

	f_V	St_{in}	St_{stag}
Top Vibrating (Bottom Fixed)	8.624	0.101	0.138
Top Vibrating (Bottom Vibrating)	11.56	0.136	0.185
Bottom Vibrating (Top Fixed)	10.28	0.121	0.165
Bottom Vibrating (Top Vibrating)	11.59	0.136	0.186

The same calculations can be done for the results of the Bottom Vibrating (Top Fixed) configuration study where the Reynolds number was increased from 3,800 to 8,300. Table 4.6 similarly shows the dominant peak frequency of motion considered the vibration frequency and the corresponding Strouhal number when considering the bundle inline or staggered. As the vortex shedding frequencies are within a similar range, the Strouhal numbers for each type of tube bundle are within 20% of each other.

Studies conducted by previous researchers during the development of tube and shell heat exchangers had led to extensive investigations on the relationship between Strouhal Number and Reynolds Number. Using the results from Table 4.6, Strouhal Numbers were plotted against Reynolds number for the inline and staggered tube bundle scenario. Figure 4.5 shows the results of this study compared to the widely accepted Strouhal Number vs Reynolds Number plot for tube vibration of circular cylinders with smooth and rough surfaces [17]. From the figure, it is clear that the Strouhal number is expected to be around 0.2 between Reynolds Number 1,000 to 10,000. The results from this study, either as an inline or staggered tube bundle, results in Strouhal numbers that are generally around this range but follow an upward trend with Re_∞.

Table 4.6 Strouhal Number for the Bottom Vibrating (Top Fixed) configuration for Re_∞ = 3,800 to 8,300 as both an inline and staggered tube bundle

Re_∞	f_V	St_{in}	St_{stag}
3,800	10.284	0.248	0.221
4,700	9.172	0.221	0.198
5,600	9.728	0.235	0.209
6,600	10.284	0.248	0.221
7,500	10.284	0.248	0.221
8,300	10.839	0.262	0.233

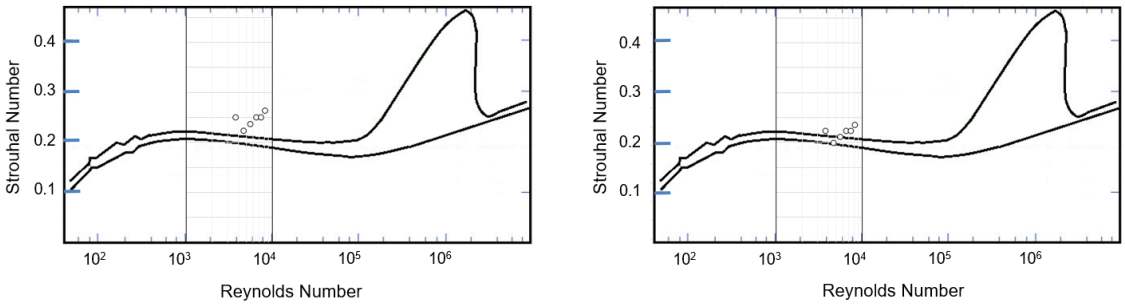

(a) **(b)**

Figure 4.5 Strouhal Number vs Re_∞ for the tube bundle when it is considered (a) inline and (b) staggered

While Figure 4.5 shows the trend for the vibration circular cylinders, Weaver's equations for Strouhal Number, given in Equations 1.4 to 1.6, were created specifically for tube bundles, using the pitch to diameter ratio of the bundle instead of the vibration frequency. Looking at the geometry when it is most staggered, Equations 1.5 was selected to calculate the Strouhal number due to the closest orientation to the tube bundle. The corresponding Strouhal Number for each tube bundle orientation is given in Table 4.7. Experiments conducted by Blevins, Chen, Pettigrew & Gorman, Polak and Weaver, Prince & Zahn, Zukauskas and Ulinskas, and Zaida for tube bundle vibration were summarized and plotted with trend lines by Zaida [58]. An adapted version showing only the trendlines for the St_1 and St_2, corresponding to one-dimension and two-dimension vibration is shown in Figure 4.6 with the results from Weaver's equations for this study. From the figure, the results from this study using Weaver's equations for Strouhal number follow the range and trend of the S_2 correlation between Strouhal number and pitch-to-diameter ratio.

Table 4.7 Strouhal Number calculation using Weaver's Equation for inline and staggered tube bundles

	P/D_R	St
inline	1.488	0.579
staggered	1.651	0.522

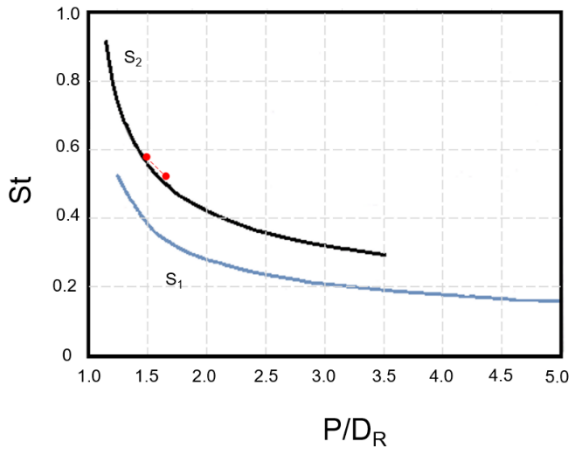

Figure 4.6 Comparison of Strouhal Number using Weaver's equation to previous experimental results for tube bundles

4.3. Fluid Elastic Instability, FEI

One of the greatest concerns for heat exchanger designers over flow-induced vibration is the transition from vortex shedding to fluid elastic instability. While vortex shedding is a well-structured fluid phenomenon that adds to the turbulence in the system, therefore aiding in heat transfer, fluid elastic instability is characterized by large bluff bodies without a consistent frequency or amplitude. Figure 4.7 shows the general relationship between the vibration amplitude and flow rate of fluid in cross-flow around tube bundles.

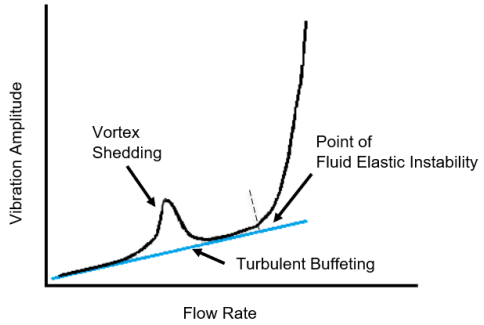

Figure 4.7 General relationship between vibration amplitude and flow rate for tube bundles

From Figure 4.7, there is a generally understood concept that at a certain flow rate, the system will become unstable and therefore the vibration amplitude will exponentially increase, leading to damage of tubes, baffles and surrounding structures. This can be avoided by not passing a critical velocity, V_{CR}. As discussed in Section 1.1, there have been multiple researchers that have developed correlations to determine the critical velocity.

4.3.1. Critical damping ratio, damping parameter & effective mass

Before the correlations to determine the critical velocity can be used, there are specific parameters of the system that are crucial to the calculation of the critical velocity of the system. The critical damping ratio, ζ, can be determined experimentally from the natural frequency. As described in Section 3.4, the natural frequency of the system was found experimentally by determining the settling time of the system in a still body of the working fluid. Curve fitting the peaks of the settling time into Equation 4.3,

yields a factor, B. From this factor, Equation 4.4 can be used to experimentally determine the critical damping ratio, and subsequently, the damping parameter, δ [31]. Table 4.8 shows the experimentally determined critical damping ratio, ζ, and damping ratio, δ.

$$y = Ce^{-Bx} \quad \text{Eq 4.3}$$

$$\zeta = \frac{-B}{2\pi f_N} \quad \text{Eq 4.4}$$

Table 4.8 Experimentally determined critical damping ratio and damping parameter for the system

	Water
f_N (Hz)	7
ζ	0.032
δ	0.201

Another parameter that is used to determine the critical velocity is the effective mass per unit length, m, of the vibration system. Equation 4.5 shows the definition of the effective mass per unit length for a single tube in a tube bundle where the density of the fluid, ρ, and the density of the tube, ρ_t, are taken into consideration. The effective mass per unit length is a function of all the contributing factors of the system. Typically for a heat exchanger design, this includes three parameters, the surrounding flow, the tube and the flow within the tube. As this is a model and we do not have internal flow within the tube, the effective mass per unit length only has two components, as shown in Equation 4.5. Within the term for the surrounding flow, the parameter C_m represents the added mass based on the flow regime. Blevin's correlation for added mass, C_m, for single phase flow is given by Equation 4.6.

$$m = \frac{\pi D^2 C_m \rho}{4} + \frac{\pi D^2 \rho_t}{4} \quad \text{Eq 4.5}$$

$$C_m = \frac{\left[\left(1+0.5\frac{P}{D}\right)\frac{P}{D}\right]^2 + 1}{\left[\left(1+0.5\frac{P}{D}\right)\frac{P}{D}\right]^2 - 1} \quad \text{Eq 4.6}$$

Using the pitch to diameter ratio when the tube bundle is most staggered, P/D = 1.664, the added mass, C_m is 1.24117. Therefore, the effective mass per unit length, m, is 0.479 kg/m. The following sections discuss the various equations for critical velocity in order avoid the onset of fluid elastic instability. Fluid elastic instability occurs when the critical velocity is larger than the gap velocity, therefore operating conditions of the system should stay with $V_{CR} > V_g$.

4.3.2. Chen's Critical Velocity Criterion [12]

Chen was one of the first researchers to create a criterion for the limitations of the critical velocity. He based his correlation, Equation 1.8, on the available experimental data at the time and chose the lowest possible velocity for a conservative value. His correlation accounts for different tube bundle arrangements. Based on the geometry, the values of a and b change. Therefore, the calculation for critical velocity can be done for the geometry as an inline or staggered tube bundle, as presented in Table 4.9. Some years later, he revised his correlation to further account for tube bundles including the pitch to diameter ratio of staggered tube bundles. This new criterion, Equation 4.7, uses the same factors based on tube bundle geometry but results in a higher critical velocity, as seen in Table 4.9.

$$\frac{V_{CR}}{f_N D} = A\left(\frac{P}{D} - 0.5\right)\left(\frac{m\delta}{\rho D^2}\right)^B \quad \text{Eq 4.7}$$

Table 4.9 Chen Calculation for Critical Velocity, V_{CR}

	A	B	V_{CR} (m/s)
Chen (Eq 1.8), inline	2.1	0.15	0.202
Chen (Eq 4.7), inline	2.1	0.15	0.234
Chen (Eq 1.8), staggered	2.8	0.17	0.264
Chen (Eq 4.7), staggered	2.8	0.17	0.306

4.3.3. Au Yang et al. & Pettigrew Critical Velocity Criteria [11]

Due to the conservative nature of the critical velocity calculation from Chen's criteria, other researchers have also proposed their own criteria to avoid fluid elastic vibration. These criteria also use the same parameters but with the constants of the equation changed based on the tube bundle geometry. Au Yang et al. proposed a criterion for the critical velocity for tube bundles when the damping parameter, δ, fits the parameter $m\delta/\rho D^2 > 0.7$ and will be conservative when < 0.7 [11].

$$\frac{V_{CR}}{f_N D} = K\left(\frac{m\delta}{\rho D^2}\right)^a \qquad \text{Eq 4.8}$$

$$\frac{V_{CR}}{f_N D} = 3.0\left(\frac{m\delta}{\rho D^2}\right)^{0.5} \qquad \text{Eq 4.9}$$

Table 4.10 Critical Velocity calculations using Au Yang et al. and Pettigrew & Taylor's criteria

	K	a	V_{CR} (m/s)
Au Yang at al., inline	3.4	0.5	0.241
Au Yang et al., staggered	4.0	0.5	0.278
Pettigrew & Taylor, all	3.0	0.5	0.212

Pettigrew & Taylor conducted a study of flexible tube bundles within single phase cross-flow. They developed their own criteria from ~ 300 experimental data points to create a general acceptance criterion. Equation 4.9 shows the equation that can have slight variance depending on the geometry. Table 4.10 also shows the critical velocity as calculated by using the general equation by Pettigrew & Taylor.

4.3.4. System Stability

Looking at the results of the critical velocity calculations, as determined by the experimentally developed criterion, in Table 4.9 and 4.10, the range is from 0.20 m/s to 0.31 m/s. When comparing these values to the gap velocities calculated for the tube bundle, inline and staggered, Vg is between 0.66 m/s and 0.74 m/s. Therefore, for Re_∞ = 7,500, the equations suggest that we are in the fluid elastic instability range.

A stability parameter check that is suggested in the ASME Code, Section III is given by the factors below and using Equation 4.8 [12].

$$\delta = 0.015$$

$$K = 2.1 \quad a = 0.5$$

Using these constants, the conservative critical velocity, $V_{CR,\,CON}$, for the system is 0.04 m/s. Comparing this value to the calculated staggered tube bundle gap velocity, V_g

= 0.743 m/s would indicate that the tests ran at Re_∞ = 7,500 are very much in the unstable region and the flow experienced is within the fluid elastic instability region. A visual representation of the experimental location is shown in Figure 4.8.

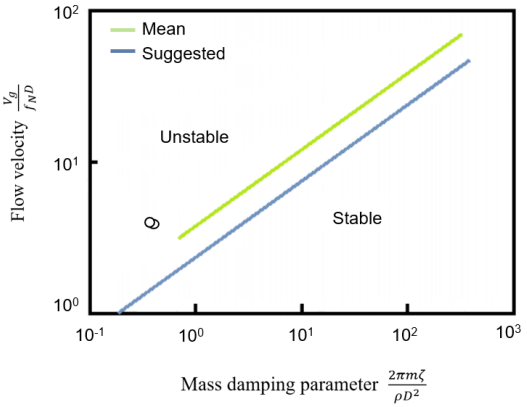

Figure 4.8 Stability diagram for the flow over tube bundles as a function of the mass damping parameter

While the results from the critical velocity calculations all suggest that the system is in the fluid-elastic instability region, the amplitude of the displacement, taken from data presented in Section 3.3 is plotted in Figure 4.9. Comparing the data and the flow rate vs vibration amplitude map, it does not agree with the exponential increase of vibration amplitude expected in the fluid elastic instability region. Instead, the trend seems to follow the vortex shedding region. Unfortunately, due to the limited size of the Reynolds number region, Re_∞ = 3,800 to 8,300, for all the tests conducted, a more inclusive flow rate map could not be created. Therefore, based on the fluid induced vibration results presented from the study, one could determine that the system is not

well represented from the critical velocity criteria. Nevertheless, a more in depth look at the surround flow features will allow the study to have a more certain conclusion.

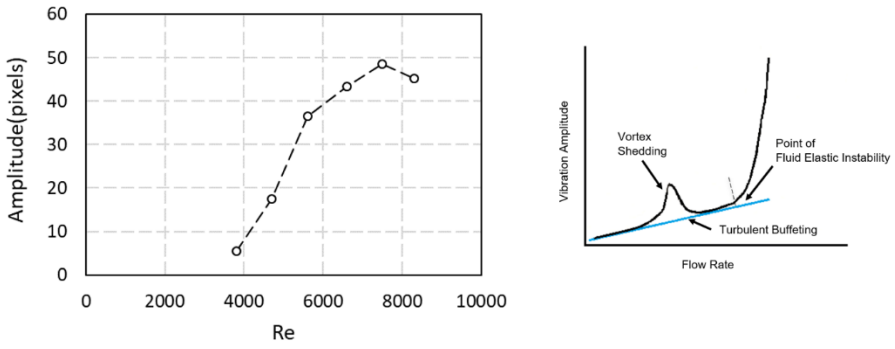

Figure 4.9 Amplitude vs Re_{∞} from the Experimental Results

5. CONCLUSION

5.1. Summary

The increased interest in complex tube and shell heat exchanger geometries for nuclear applications has opened new areas of interest in analysis. While increased turbulence within the shell side flow is encouraged, flow-induced vibration is a potential concern for tube breakage and costly damage. Therefore, when studying the unique geometry of a helical coil heat exchanger, particular attention must be given to the design of the support structures that avoid flow-induced vibration. A way to know how to design the heat exchanger is to know the limits and characterization of the vibration. Therefore, the focus of this study was to model the tube and shell features of a Helical Coil Heat Exchanger for a single and adjacent tubes to have self-induced vibration allowances in two-dimensions. Modules that allowed the two-dimensional vibration were designed and 3-D printed. These modules housed springs to simulate the support structures around tubes meant to dampen vibration and acted as viewing ports for data acquisition.

The vibration of the single and adjacent tube vibration was experimentally captured using a high-speed camera. Images captured at 1,000 fps for ~ 10 seconds, analysis using Hough Transform to track the circle center locations. Experiments looked at Rod 9 vibration alone and compared it with the vibration response when Rod 10, a downstream rod was allowed to vibrate. Similarly, Rod 10 vibration was studied before and after the addition of an upstream rod allowed to vibrate. Experiments also looked at the effect of increasing Reynolds number. For the particular configuration where Rod 9

was fixed and Rod 10 was allowed to vibrate, experiments captured the vibration motion of the rod from Re_∞ = 3,800 to 8,300. From these experiments the following observations were drawn for the flow-induced vibration of a single and adjacent tubes within the model HCHX design of this study.

5.2. Conclusions

The results of this study show that different configurations, meaning the addition of an upstream or downstream tube that is allowed to vibrate, will change the frequency and amplitude of the tube. Studies have previously made note of the influence of upstream flow features of the system impacting the later tube rows. This is exemplified by the various correlations that divide the tube bundle into two regions, the "first few rows" and the "middle of the bundle." From this study, Figure 4.1 shows the influence that the addition of a downstream vibrating tube can have on the monitored tube. Nevertheless, less research has focused and compared the effect of a downstream tube on an upstream's tube vibration. Figure 4.2 shows the effect of the monitored tube when an upstream tube is allowed to vibrate. The upstream tube is an adjacent tube, therefore, the formation of the flow structures between the tubes can be understood dependent on both tubes. Regardless of addition upstream or downstream, the results show that the frequency of the motion changes. The frequency of a system with circular cylinders is considered relatively steady, as shown in the flow maps in Figure 4.5. A change in frequency represents a shift of the energy that is being absorbed by the monitored tube.

Therefore, when an adjacent tube is allowed to vibrate, the results in Figure 4.1 and 4.2 show that the tube increases in vibration frequency but its amplitude becomes steadier.

A change in the frequency of the vibration of a tube is considered significant to the system, because as this study shows, the vibration frequency varies very minimally with changes in flow rate. For the experiments conducted at incrementally increasing Reynolds number, the frequency of motion did not vary more than 2 Hz. Nevertheless, the shape and amplitude of the motion were directly related to the increase in Reynolds number.

Examining the results with the Strouhal number, there is agreement with equations for general circular cylinder vibration where the Strouhal number should be ~ 0.2 using the vibration frequency. The trend of the Strouhal Number as a function of Reynolds Number map does not match the trend in the experiments conducted. Nevertheless, when Weaver's correlation for staggered tube bundles is used, which eliminates the dependence on the frequency vibration and determines Strouhal Number directly from the tube bundle geometry, the results in Figure 4.6 show agreement with their Strouhal vs Reynolds number plots. Weaver's correlation was created directly from experiments from tube bundles while the general circular cylinder trends use data from single vibrating tubes to tube of different materials.

The final part of the study examined the current existing criteria for avoiding the point of fluid elastic instability within the system. Determining the natural frequency and mass damping parameters experimentally, criteria from Chen, Au Yang et al. and Pettigrew and Taylor were used to calculate a critical velocity. From all the equations,

the critical velocity is predicted to be in the 0.2 to 0.3 m/s range. Experiments conducted at Re_∞ = 7,500 have a calculated gap velocity of 0.74 m/s. Therefore, meaning that based on these criteria, the system is well within the fluidelastic instability region. Comparing the vibration amplitude map against the trend for tube bundles, the results from the experiments do not agree that the system is in the fluid elastic instability region.

5.3. Future Work

The purpose of this study was to investigate the vibration of tubes within a unique tube bundle configuration when an adjacent tube is allowed to vibrate. Results showed that having an adjacent tube will change the frequency and amplitude of the vibration. Therefore, when designers are looking at the areas of highest concern for the potential for flow induced vibration, it can be suggested that allowing more than one tube in the area to vibrate can in fact reduce the overall potential for damage. Due to the limitations of this study, which examined a pair of tubes from a much larger system, there is a need for characterizing the vibration of the particular system. Future work will include monitoring tubes from different areas around the complex geometry to have a better understanding of the effect of vibration of tubes both upstream, downstream and adjacent to a tube that is vibrating. This will provide designers the capability to create safer and more effective heat exchangers.

REFERENCES

1. D.G. Prabhanjan, V.G.S. Raghavan, and T.J. Rennie, "Comparison of heat transfer rates between a straight tube heat exchanger and a helically coiled heat exchanger," *Int. Communications in Heat and Mass Transfer*, **29**(2), pp.185 (2002). doi:10.1016/S0735-1933(02)00309-3
2. IAEA, *Innovative Small and Medium Sized Reactors: Design Features, Safety Approaches and R&D Trends, Tech. Rep. IAEA-TECDOC-1451*, International Atomic Energy Agency, Vienna Austria (2005).
3. N.V. Hoffer, N.A. Anderson, and P. Sabharwall, "Development and Transient Analysis of a Helical-coil Steam Generator for High Temperature Reactors," *Journal of Young Investigators,* **22** (2), pp. 40-50 (2011).
4. E.K. Kim, and S.O. Kim, "Sodium-Cooled Fast Reactor Helical Coil Steam Generator," *Transactions of the Korean Nuclear Society Autumn Meeting*, Jeju, Korea, October 21-22, 2010, pp.47 (2010).
5. J.N. Reyes Jr., "NuScale Plant Safety in Response to Extreme Events," *Nuclear Technology*, **178**, pp. 153-163 (2017). doi: 10.13182/NT12-A13556
6. M. Delgado, Y.A. Hassan, N.K. Anand, "Experimental flow visualization study using particle image velocimetry in a helical coil steam generator with changing lateral pitch geometry," *Int. Journal of Heat and Mass Transfer*, **133**, pp. 756-768 (2019). doi: 10.1016/j.ijheatmasstransfer.2018.12.152
7. M. Delgado, G.A. Porter, Y.A. Hassan, N.K. Anand, "Experimental shell-side surface pressure measurements on tubes within a model helical coil heat exchanger," *Nuclear Engineering and Design*, **370**, pp. 110906 (2020). doi: 10.1016/j.nucengdes.2020.110906
8. A.A. Zukauskas and R. Ulinskas, Heat Transfer in Tube Banks in Crossflow, New York: Hemisphere (1988).
9. K.P Singh, and S.I Soler, Mechanical Design of Heat Exchangers and Pressure Vessel Components, Cherry Hill, NJ: Arturus, 1984.
10. J.P Gupta, Fundamentals of Heat Exchanger and Pressure Vessel Technology, Washington DC: Hemisphere, pp. 316-348 (1989).
11. K. Thulukkanam, *Heat Exchanger Design Handbook*, 2 ed., Boca Raton: Taylor & Francis Group LLC (2013). Print.
12. S. Kaneko, T. Nakamura, F. Inada, M. Kato, K. Ishihara, T. Nishihara, *Flow-Induced Vibrations: Classifications and Lessons from Practical Experiences*, 2 ed., London: Academic Press (2014). Print.
13. Y.N. Chen and M. Weber, "Flow induced vibrations in tube bundle heat exchangers with crossflow and parallel flow," in Flow Induced Vibrations in Heat Exchangers, Proceedings of a Symposium Sponsored by the ASME, New York, pp. 57-77 (1970).
14. Y.N. Chen, Flow Induced Vibration and Noise in Tube Bank Heat Exchangers due to Von Karman Streets, Trans. ASME Journal of Engineering for Industry, **90**, pp. 134-146 (1968).

15. J.S. Fitz-Hugh, Flow Induced Vibration in Heat Exchangers, International Symposium of Vibration Problems in Industry, Keswick, U.K, April 10-12 1973.
16. D.S Weaver, J.A. Fitzpatrick, M.L, El Kashlan, Strouhal Number of Heat Exchangers tube Arrays in Crossflow, ASME Symposium on Flow Induced Vibration, Chicago, IL, **104**, 1986.
17. R.D Blevins, Flow Induced Vibration, 2 ed., New York: Van Nostrand Reinhold (1990). Print.
18. A.A. Zukauskas, Vibration of tubes in heat exchangers, in High-Performance Single-Phase Heat Exchangers, Washington: Hemisphere (1989).
19. P.R. Owen, Buffeting excitation of boiler tube vibration, Journal of Mechanical Engineering Science, **7**(4), (1965).
20. D.S Weaver and L.K Grover, Crossflow Induced Vibration in a Tube Bank – Turbulent Buffeting and Fluid Elastic Instability, Journal of Sound Vibration, 59(2), pp.277-294 (1978).
21. M.P. Paidoussis "Real-life experiences with flow-induced vibration," Journal of Fluids and Structures, **22** (6-7), pp. 741-755 (2006).
22. J.H Connors Jr., Fluid Elastic Vibration of Tube Arrays Excitation by Crossflow, Flow Induced Vibration in Heat Exchangers (D.D Reill, ed.), ASME, New York, pp. 42-56 (1970).
23. S.S Chen, Flow Induced Vibration of Circular Cylindrical Structures, Argonne National Laboratory, Report No. ANL-CT-85-51, Argonne, IL (1985).
24. M.K. Au-Yang, R.D. Blevins, and T.M. Mulcahy, "Flow Induced Vibration Analysis of Tube Bundles – A proposed Section III Appendix N nonmandatory code," Journal of Pressure Vessel Technology, 113, pp. 257-267 (1991).
25. M.J Pettigrew and C.E. Taylor, "Fluid Elastic Instability of Heat Exchanger Tube Bundles: Review and Design Recommendations," Journal of Pressure Vessel Technology, 113, pp.242 -255 (1991).
26. S.P Timoshenko and D. H Young, "CH.5 Vibration problems in engineering," in *Vibration of Elastic-Bodies*, Toronto: VanNostrand Reinhold (1965).
27. D.S. Weaver, S. Zaida, M.K. Au-Yang, S.S. Chen, M P. Paidoussis, M.J. Pettigrew, "Flow-Induced Vibrations in Power and Process Plant Components – Progress and Prospects," J. Pressure Vessel Technology, **122(3)**, pp. 339-348 (2000). doi: 10.1115/1.556190.
28. F. Inada, K. Kawamura, A. Yasuo, K. Yoneda, "An experimental study on the fluidelastic forces acting on a square tube bundle in two-phase cross-flow," *J. of Fluids and Structures*, **16(7)**, pp. 891 – 907, (2002). doi:10.1006/jfls.460.
29. F. Inada, T. Nishihara, A. Yasuo, R. Morita, A. Sakishita, J. Mizutani, "Self-excited vibration of cross-shaped tube bundle in cross-flow," J. of Fluids and Structures, 18(5), pp. 651 – 661 (2003). doi: 10.1016/j.jfluidstructs.2003.07.015.
30. H.G.D. Goyder, "An assessment method for unstable vibration in multispan tube bundles," J. of Fluids and Structures, 18(5), pp. 555-572 (2003). doi: 10.1016/j.jfluidstructs.2003.08.012
31. I. Catton, V.K. Dhir, D. Mitra, O. Alquaddoomi, P. Adinolfi, "Development of Design Criteria for Flow Induced Structural Vibrations in Steam Generators and Heat

Exchangers," United States: DE- FG03- 00SF22169, (2004). Web. doi: 10.2172/822365.
32. T.K. Lin, M.H. Yu, "An experimental study on the cross-flow vibration of a flexible cylinder in cylinder arrays," Experimental Thermal and Fluid Science, 29(4), pp. 523 – 536 (2005). doi: 10.1016/j.expthermflusci.2004.06.004.
33. M.P. Paidoussis, "Real-life experiences with flow-induced vibration," J. of Fluids and Structures, 22(6-7), pp. 741-755 (2006). doi: 10.1016/j.jfluidstructs.2006.04.002.
34. T. Sawadogo, N. Mureithi, "Fluidelastic instability study in a rotated triangular tube array subjected to two-phase cross-flow. Part I: Fluid force measurements and time delay extraction," J. of Fluids and Structures, 49, pp. 1-15 (2014). doi: doi.org/10.1016/j.jfluidstructs.2014.02.004.
35. K.L. Annamalai, K.S.K. Karuppasamy, "Experimental investigation on stability of an elastically mounted circular tube under cross flow in normal triangular arrangement," Journal of Vibroengineering, 18 (3), (2016). doi: 10.21595/jve.2016.16708.
36. W.R. Marcum, P.L. Harmon, "Characterizing fluid structure interactions of a helical coil in cross flow," J. of Fluids and Structures, 65, pp. 355 – 380 (2016). doi: 10.1016/j.jfluidstructs.2016.06.008.
37. A. Elhelaly, M. Hassan, A. Mohany, S. Moussa, "An Experimental Investigation of the Dynamics of a Loosely Supported Tube Array," Proceedings of the ASME 2017 Pressure Vessels and Piping Conference. Volume 4: Fluid-Structure Interaction. Waikoloa, Hawaii, USA. July 16–20, 2017. ASME. (2017). doi: 10.1115/PVP2017-65898.
38. H. Yuan, J. Solberg, E. Marzari, A. Kraus, I. Grindeanu, "Flow-induced vibration Flow-induced vibration analysis of a helical coil steam generator experiment using large eddy simulation," Nuclear Engineering and Design, (322), pp. 547-562 (2017). doi: 10.1016/j.nucengdes.2017.07.029.
39. B.L. da Silva, R. D. Luciano, J. Utzig, H. F. Meier, "Flow patterns and turbulence effects in large cylinder arrays," Int. J. of Heat and Fluid Flow, 69, pp. 136-149 (2018). doi: 10.1016/j.ijheatfluidflow.2017.12.013.
40. W. Chen, C. Ji, J. Williams, D. Xu, L. Yang, Y. Chi, "Vortex – induced vibrations of three tandem cylinders in laminar cross-flow: Vibration response and galloping mechanism," 78, pp. 215 – 238 (2018). doi: 10.1016/j.jfluidstructs.2017.12.017.
41. D. Yin, E. Passano, C. M. Larsen, "Improved In-Line Vortex Induced Vibrations Prediction for Combined In-Line and Cross-Flow Vortex-Induced Vibrations Responses," J. of Offshore Mechanics and Arctic Engineering, 140(3), (2018). doi: 10.1115/1.4038350.
42. A. Cioncolini, J. Silva-Leon, D. Cooper, M. K. Quinn, H. Iacovides, "Axial-flow-induced vibration experiments on cantilevered rods for nuclear reactor applications," Nuclear Engineering and Design, 338, pp. 102-118 (2018). doi: 10.1016/j.nucengdes.2018.08.010.
43. R. Alvarez-Briceno, F.T. Kanizawa, G. Ribatski, L.P.R. de Oliveira, "Validation of turbulence induced vibration design guidelines in a normal triangular tube bundle during two-phase crossflow," J. of Fluids and Structures, 76, pp. 301 – 318 (2018). doi: 10.1016/j.jfluidstructs.2017.10.013.

44. Q. Han, Y. Ma, W. Xu, S. Zhang, “An experimental study on the hydrodynamic features of two side-by-side flexible cylinders undergoing flow-induced vibrations in a uniform flow,” Marine Structures, 61, pp. 326-342 (2018). doi: 10.1016/j.marstruc.2018.06.001.
45. D. Tang, S. Bao, B. Lv, H. Cui, L. Luo, M. Xu, “Investigation of shedding patterns and its influences on lift performance of a cylinder bundle in cross flow,” J. of Mechanical Science and Technology, 33(6), pp. 2651 – 2663 (2019). doi: 10.1007/s12206-019-0513-9.
46. E. Wang, W. Xu, Y. Yu, L. Zhou, A. Incecik, “Flow-induced vibrations of three and four long flexible cylinders in tandem arrangement: An experimental study,” Ocean Engineering, 78, pp. 170-184 (2019). doi: 10.1016/j.oceaneng.2019.02.053.
47. D. Tang, D. Liu, Z. Ding, H. Zhu, W. Yuan, “Numerical investigation on the interactions of flow induced vibrations among neighboring cylinders in a cylinder bundle,” Annals of Nuclear Energy, 140, pp. 107156 (2020).
48. G. F. Hewitt, G.L. Shires, T.R. Bott, Process Heat Transfer, Boca Raton: CRC Press, Inc. (1994).
49. A. O. Fredheim, “Thermal Design of Coil-Wound LNG Heat Exchangers: Shell-Side Heat Transfer and Pressure Drop,” (NTIS Issue No. 199520) [Doctoral Dissertation, The University of Trondheim]. National Technical Reports Library. https://ntrl.ntis.gov/NTRL/dashboard/searchResults/titleDetail/DE95772442.xhtml
50. B.O. Neeraas, A.O. Fredheim, B. Ajunan, “Experimental shell-side heat transfer and pressure drop in gas flow for spiral-wound LNG heat exchanger,” Int. J. of Heat and Mass Transfer, 47, pp. 353 – 361 (2004). doi: 10.1016/S0017-9310(03)00400-9.
51. J. M Bourguet, “Cryogenic Technology and Scaleup Problems of Very Large LNG Plants,” In: Timmerhaus K.D. (eds) Advances in Cryogenic Engineering, vol 18. Springer, Boston, MA. (1973). doi:10.1007/978-1-4684-3111-7_2
52. D. Tochio, S. Nakagawa, “Thermal Performance of Intermediate Heat Exchanger during High-Temperature Continuous Operation in HTTR,” J. of Nuclear Science and Technology, 48(11), pp. 1361-1368 (2011). doi: 10.1080/18811248.2011.9711828
53. M.C. Weikl, K. Braun, J. Weiss, “Coil-wound Heat Exchangers for Molten Salt Applications,” Energy Procedia, 49, pp. 1054 – 1060 (2014). doi: 10.1016/j.egypro.2014.03.113
54. M. Lazova, H. Huisseune A. Kaya, S. Lecompte, G. Kosmadakis, M. De Paepe, “Performance Evaluation of a Helical Coil Heat Exchanger Working under Supercritical Conditions in a Solar Organic Rankine Cycle Installation,” Energies, MDPI Open Access Journal, 9(6), pp. 1 – 20 (2016). doi: 10.3390/en9060432
55. NuScale Power LLC., “Chapter 5: Reactor Coolant Systems and Connecting Systems” NuScale Standard Plant Design Certification Application, Rev 5, July 2020. <https://www.nrc.gov/docs/ML2022/ML20224A493.pdf>.
56. R.D Mehta, and P. Bradshaw, “Design rules for small low speed wind tunnels,” The Aeronautical Journal of the Royal Aeronautical Society, 718, pp. 443 – 449, (1979).
57. “imfindcircles,” Help Center: Support: Documentation, MathWorks®, https://www.mathworks.com/help/images/ref/imfindcircles.html

58. S. Zaida, “Vorticity shedding and acoustic resonance in tube bundles,” Journal of the Brazilian Society of Mechanical Sciences and Engineering, 28(2), pp. 186 – 189 (2006). doi: 10.1590/S1678-58782006000200008

APPENDIX

Tracking Code for Single Rod

```
clc; clear all; close all; tic;
data_dir = 'G:\FIV Images\Nov 30 Bottom Images\SB 45 Hz Set1 Edit2\';
images = dir([data_dir '*.tif']);
position = zeros(size(images,1),2);
out_dir = 'G:\FIV Images\Nov 30 Bottom Images\';
%mkdir(out_dir);
outfile = 'SB 45 Track1.xlsx';
parfor i = 1:size(images,1)
   fprintf('Image %d\n\n', i);
   frame = imread([data_dir images(i).name]);
   [centers, radii, metric] = imfindcircles(frame, [400 550],'sensitivity', 0.998,
'ObjectPolarity', 'dark');
   if ~(isempty(centers))
      position(i,:) = centers(1,1:2);
   end
end
clc
time = toc;
fprintf('Average Frame Computation Time: %dms',
round(time*1000/size(images,1)));
%%
fprintf('\n\nSaving Position File...\n');

relative_pos = [position(:,1) - position(1,1) position(:,2) - position(1,2)];
xl_mat = cell(size(images,1)+1,5);
xl_mat(1,:) = [{'Frame'},{'position x'},{'position y'},{'displacement
x'},{'displacement y'}];
xl_mat(3:size(xl_mat,1),1) = num2cell(1:size(images,1)-1)';
xl_mat(2:size(xl_mat,1),2:3) = num2cell(position);
xl_mat(2:size(xl_mat,1),4:5) = num2cell(relative_pos);
xlswrite([out_dir outfile],xl_mat);
plot(position);

fprintf('\nAll Done Here :)\n\n');
```

Tracking Code for Two Rods in Same Image

```
clc; clear all; close all; tic; clf;
data_dir = 'G:\Calibration FIV\Double bottom\DB Air Edit1\';
images = dir([data_dir '*.tif']);
position = zeros(size(images,1),4);
out_dir = 'G:\Calibration FIV\Double bottom\';
%mkdir(out_dir);
outfile = 'CAL D Air Track1.xlsx';
parfor i = 1:size(images,1)
   fprintf('Image %d\n\n', i);
   frame = imread([data_dir images(i).name]);
   temp_pos = zeros(2,2);

   for j = 1:2
      window = frame((1+size(frame,1)/2*(j-1)):(size(frame,1)*j/2),:,:);
      [centers, radii, metric] = imfindcircles(window, [160 180],'sensitivity',
0.999, 'ObjectPolarity', 'dark');
      if size(centers,1)>0
         temp_pos(j,:) = [centers(1,1) centers(2,2)+(j-1)*size(frame,1)/2];
      end
   end
   position(i,:) = [temp_pos(1,:) temp_pos(2,:)];
end
clc
time = toc;
fprintf('Average Frame Computation Time: %dms',
round(time*1000/size(images,1)));
%%
fprintf('\n\nSaving Position File...\n\n');

relative_pos = [position(:,1) - position(1,1) position(:,2) - position(1,2)
position(:,3) - position(1,3) position(:,4) - position(1,4)];
xl_mat = cell(size(images,1)+1,9);
xl_mat(1,:) = [{'Frame'},{'position x'},{'position y'},{'position x'},{'position
y'},{'displacement x'},{'displacement y'},{'displacement x'},{'displacement y'}];
xl_mat(3:size(xl_mat,1),1) = num2cell(1:size(images,1)-1)';
xl_mat(2:size(xl_mat,1),2:5) = num2cell(position);
xl_mat(2:size(xl_mat,1),6:9) = num2cell(relative_pos);
xlswrite([out_dir outfile],xl_mat);
plot(position);
fprintf('All Done Here :)\n\n');
```

FFT and PSD Plotting

```
%FFT
clc;
close all;
clear;
% Read data from file
data_name = 'D:\HCSG4\Results& Data\For Dissertation\Natural
Frequency\FIV_CalibBox_Air&Water.csv';
temp = dlmread(data_name, ',', 1, 0);
% Data consist time and position
time = temp(:,1);
P = temp(:,4);
% Get fluctuation component of data by substract mean value and normalized
% by standard deviation
pprime = (P - mean(P))/ std(P);
% Data size, number of samples
L = size(time,1);
% data sample inverval, used to calculate frequency
dt = time(2) - time(1);
% sample frequency
Fs = 1.0/dt;
% Fill data size to be power of 2, improve calculation efficiency
NFFT = 2^nextpow2(L);
% FFT Calculation
Y = fft(pprime, NFFT);
% Frequency vector
f = Fs*(0:(NFFT/2))/NFFT;
P2 = abs(Y/NFFT);       % Two-sided spectrum
P1 = 2*P2(1:NFFT/2+1);  % Single-sided spectrum
% Normalized FFT results
P_norm = P1 ./max(P1);

% Figure 1, FFT
figure(1);
plot(f,P_norm);
title('FFT Plot of Sample Signals');
xlabel('Frequency (Hz)', 'FontSize',12,'FontWeight','bold');
ylabel('|P(t)|', 'FontSize',12,'FontWeight','bold');
set(gca,'TickDir','out','FontSize',12,'FontWeight','bold');
% Set custom range of plots
set(gca,'Xlim',[0 500]);
%% PSD calculation using Welch's function
%  PSD: Power Spectral Density
```

```
w_l = 1000; %window length
w_l_o =200; %window length overlapping
% Px_50GPM(:,i),w_x_50GPM(:,i)] =
pwelch(vel_pt_x_50GPM(:,i),w_l,w_l_o,length(vel_pt_x_50GPM(:,i)),freq_50GPM,'on
esided');
% [pxx,freq] = pwelch(pprime,[],[],[],Fs,'onesided','psd');
[pxx,freq] = pwelch(pprime,w_l,w_l_o,length(pprime),Fs,...
   'ConfidenceLevel', 0.98);
%'onesided','psd'
findpeaks(pxx,freq,'MinPeakDistance',10);
[pks,locs, w, p] = findpeaks(pxx,freq)
%%
% PSD plot
figure(2);
loglog(freq, pxx);
title('PSD plot using Welch function');

set(gca,'XScale',  'log', 'YScale', 'log', ...
       'YGrid', 'off', 'XGrid', 'on', ...
       'TickDir','out','FontSize',12,'FontWeight','bold');
```

FEA Sensitivity Data

Solidworks 2018							
Name of Part	Rod Support_Single3.sldprt						
Material	AISI 316 Annealed Stainless Steel Bar				Yield Strength	1.38E+08	
Fixtures	one end perfect fix						
	one face with 65.9 psi						
All Solid Standard Mesh							
Study	1	2	3	4	5	6	7
Element Size (in)	0.0932537	0.0817566	0.0664273	0.0479043	0.0376847	0.0319362	0.025549
Total Nodes	2096	3125	5463	12797	25181	39666	74356
Total Elements	1216	1905	3410	8387	16928	27084	51543
Max Aspect Ratio	2.9719	3.1143	3.0131	25.352	32.424	27.339	25.693
% with AR < 3				99.7	99.4	99.9	99.9
Maximum Stress (vonMises)	1.17E+07	1.17E+07	1.20E+07	1.31E+07	1.31E+07	1.37E+07	1.42E+07
Maximum Displacement (mm)	2.501	2.513	2.527	2.546	2.55	2.551	2.551
Maximum Strain	4.37E-05	4.57E-05	4.82E-05	4.87E-05	5.29E-05	5.35E-05	5.92E-05